

DIRECT SOLAR ABSORPTION NANOPARTICLE DOPED MEMBRANES FOR A  
HYBRID MEMBRANE DISTILLATION AND PHOTOVOLTAIC CELL

by

Alejandro Espejo Sanchez



A thesis

submitted in partial fulfillment

of the requirements for the degree of

Master of Science in Mechanical Engineering

Boise State University

December 2020

© 2020

Alejandro Espejo Sanchez

**ALL RIGHTS RESERVED**

BOISE STATE UNIVERSITY GRADUATE COLLEGE

**DEFENSE COMMITTEE AND FINAL READING APPROVALS**

of the thesis submitted by

Alejandro Espejo Sanchez

Thesis Title: Direct Solar Absorption Nanoparticle Doped Membranes for a Hybrid Membrane Distillation and Photovoltaic Cell

Date of Final Oral Examination: 17 November 2020

The following individuals read and discussed the thesis submitted by student Alejandro Espejo Sanchez, and they evaluated her presentation and response to questions during the final oral examination. They found that the student passed the final oral examination.

Todd Otanicar, Ph.D. Chair, Supervisory Committee

John Gardner, Ph.D. Member, Supervisory Committee

Mahmood Mamivand, Ph.D. Member, Supervisory Committee

The final reading approval of the thesis was granted by Todd Otanicar, Ph.D., Chair of the Supervisory Committee. The thesis was approved by the Graduate College.

## DEDICATION

I want to dedicate this work to my family, especially my parents Maria and Jesus, for their continuous support of my education and life goals. Coming to the US several years ago was a difficult decision, but they have supported me in every step of the way. They taught me the work ethic and perseverance that has taken me so far. I also want to dedicate this work to my girlfriend, Patrizia, who has permanently supported me through all the stressful moments of this process. You push me to try my best and to be a better person every day.

## ACKNOWLEDGMENTS

Special thanks to my fellow lab members and especially to Dr. Todd Otanicar, thesis advisor. Dr. Otanicar's guidance, feedback, encouragement, and mentorship have been crucial in progressing my thesis over the last two and a half years.

The author would also like to acknowledge the partial support of the Department of the Interior, Bureau of Reclamation under agreement number R17AC00134 and R19AC00067.

## ABSTRACT

The growing demand for clean water supplies is driving the need for an innovative approach of water desalination. Developing a method for treating water with high salinities is possible with membrane distillation (MD). Additionally, MD is very attractive for pairing with solar energy due to the low temperature requirements. The integration of a membrane distillation system with a photovoltaic (PV) system will result in the co-production of electricity and clean water, thereby improving the economics of MD. Such a hybrid system will directly absorb thermal energy in the membrane for desalination while taking advantage of the spectrally selective nature of PV to generate electricity. At the top of the system is a PV cell that will filter the visible light wavelengths and transmit the remaining ultraviolet and infrared to a membrane doped with absorbing nanoparticles located at the core of the system. This configuration integrates the system and provides an avenue for increasing the membrane performance by mitigating the temperature polarization effect, which is the gradual decrease of temperature at the thermal boundary layers of the membrane due to the large amount of heat consumed during the phase transition process. A custom multi-step phase inversion process fabricates Polyvinylidene Fluoride (PVDF) membranes through a Diffusion Induced Phase Separation (DIPS) technique. The process allows for the addition and controlled distribution of nanoparticles at different loadings across the membrane structure. The membranes fabricated during this study exhibited a microporous, sponge-like, and hydrophobic nature during the morphological analysis. Scanning Electron

Microscopy (SEM) images and contact angle measurements above  $100^\circ$  prove the suitability for MD applications. The membranes doped with a 0.8wt% load of carbon coated copper nanoparticles increased the solar absorptance of the membrane by 80% during the optical analysis. A custom lab-scale direct contact membrane distillation (DCMD) setup characterizes the membranes fabricated off-sun and on-sun. The doped membrane exhibited a 15-32% increase in desalination performance when exposed to solar irradiance while simultaneously producing 0.36W of electrical power. The overall project led to the increased use of renewable energy for desalination while improving the ability to use MD for desalination purposes.

## TABLE OF CONTENTS

DEDICATION .....	iv
ACKNOWLEDGMENTS .....	v
ABSTRACT.....	vi
LIST OF TABLES .....	x
LIST OF FIGURES .....	xi
LIST OF ABBREVIATIONS.....	xiv
CHAPTER ONE: INTRODUCTION.....	1
1.1.    The Need.....	1
1.2.    Motivation.....	2
1.3.    Introduction to Desalination .....	2
1.4.    Introduction to Membrane Distillation (MD) .....	4
1.5.    MD Configurations .....	8
1.6.    Membrane Characteristics .....	11
Membrane Characteristics .....	11
Membrane Materials .....	15
Membrane Characterization Techniques .....	16
Membrane Fabrication Processes and Geometries .....	17
1.7.    Solar Assisted MD Background.....	19
1.8.    Study Scope and Objectives.....	25

CHAPTER TWO: MEMBRANE SYNTHESIS AND CHARACTERIZATION .....	29
2.1. Materials .....	29
2.2. Membrane Synthesis .....	32
2.3. Optical Characterization .....	37
2.4. Morphological Characterization .....	38
2.5. Optical Results .....	39
2.6. Morphological Results .....	43
2.7. Conclusions.....	49
CHAPTER THREE: HYBRID MEMBRANE DISTILLATION AND PHOTOVOLTAIC CELL SYSTEM DESIGN AND CHARACTERIZATION .....	51
3.1. DCMD Setup .....	51
3.2. Hybrid System Characterization.....	55
Solar Module Characterization .....	55
Desalination Characterization.....	57
3.3. Hybrid System Results.....	59
Solar Module Results .....	59
Desalination Results Off-Sun .....	64
Desalination Results On-Sun .....	68
3.4. Conclusions.....	77
CHAPTER FOUR: CONCLUSIONS AND FUTURE WORK.....	79
4.1 Conclusions.....	79
4.2. Future Work .....	80
REFERENCES .....	82

## LIST OF TABLES

Table 1.1.	PSD for Conventional Membrane Processes [8,21] .....	14
Table 1.2.	Properties of Polymer Materials [4,14].....	16
Table 1.3.	Summary of Previous Solar Assisted MD Performance When the Membrane is Directly Exposed to Irradiance .....	24
Table 2.1.	Summary of Membrane Fabrication Parameters .....	37
Table 2.2.	Summary of the Membrane Composition and Weighted Spectral Absorptance at Different Carbon Coated Copper Nanopowder Weight Percent Ratios .....	41
Table 2.3.	Summary of Weighted Spectral Absorptance of the Membranes Doped with Different Nanoparticles.....	43
Table 3.1.	Summary of Solar Modules Characteristics .....	56
Table 3.2.	Summary of CdTe Thin Film Solar Panels Performance Characterization .....	62
Table 3.3.	Doped Membrane (C-Cu_0.8_Y_250) and CdTe Thin Film Solar Module (CdTe_60%_225) Performances On-Sun at Standard Conditions.....	75

## LIST OF FIGURES

Figure 1.1.	Schematic Representation of Water Flux in Membrane Distillation [2,8] .	3
Figure 1.2.	Detailed Schematic Representation of the Temperature Polarization Phenomenon in MD [18,19] .....	7
Figure 1.3.	Schematic Diagrams of Common MD Configurations: DCMD, AGMD, VMD, and SGMD [2,6,9,10] .....	9
Figure 1.4.	Membrane Permeability Characterization by Contact Angle. Representation of Hydrophobic and Hydrophilic Surfaces [12].....	13
Figure 1.5.	Proposed Hybrid PV-Membrane System Design .....	26
Figure 2.1.	Commercial PVDF Membrane: a) Physical Sample, b) Spectral Optical Properties .....	31
Figure 2.2.	Schematic of Custom Phase Inversion Process .....	35
Figure 2.3.	Membranes Fabricated by Custom Phase Inversion Process: a) Plain (Plain_0.0_Y_250), b) Doped (C-Cu_0.8_Y_250).....	36
Figure 2.4.	Spectral Absorptance of the Trial Doped Membranes Fabricated via Phase Inversion .....	40
Figure 2.5.	Spectral Optical Properties of the Plain Membrane Fabricated via Phase Inversion .....	42
Figure 2.6.	Spectral Optical Properties of the Doped Membrane (0.8 wt% Copper Nanopowder Carbon Coated) Fabricated via Phase Inversion .....	42
Figure 2.7.	Spectral Absorptance Comparison Between the Plain and Doped Membranes.....	43
Figure 2.8.	SEM Images of the Plain Membrane Fabricated via Phase Inversion: a) Top Surface, b) Cross Section .....	45
Figure 2.9.	SEM Images of the Doped Membrane Fabricated via Phase Inversion: a) Top Surface, b) Cross Section .....	46

Figure 2.10.	SEM Images of a Commercial PVDF Membrane: a) Top Surface, b) Cross Section.....	47
Figure 2.11.	Membrane Contact Angle Images and Measurements: a) Plain Membrane, b) Doped Membrane, c) Commercial Membrane .....	49
Figure 3.1.	Schematic Diagram of the Proposed Experimental System Design for the Membrane Performance Characterization .....	53
Figure 3.2.	Hybrid Membrane Distillation and Photovoltaic Cell System Setup for Outdoor Performance Characterization .....	54
Figure 3.3.	Semi-transparent Solar Modules: a) CdTe_30%_721, b) CdTe_40%_900, c) CdTe_60%_225, d) Silicon_30%_144 .....	55
Figure 3.4.	Spectral Transmittance of Two Types of Solar Modules (CdTe_60%_225 and Silicon_30%_144) Used in Architectural Glass Applications .....	60
Figure 3.5.	Spectral Intensity and Transmittance of Three Semi-transparent CdTe Solar Modules (CdTe_30%_721, CdTe_40%_900, and CdTe_60%_225) .....	61
Figure 3.6.	Current-Voltage (I-V) and Power (W) Performance Curves of Three CdTe Thin Film Solar Panels: a) CdTe_30%_721; b) CdTe_40%_900; c) CdTe_60%_225 .....	63
Figure 3.7.	Plain Membrane (Plain_0.0_Y_250) Performance Off-Sun at Standard Conditions (Permeate Flux and Salt Rejection).....	65
Figure 3.8.	Doped Membrane (C-Cu_0.8_Y_250) Performance Off-Sun at Standard Conditions (Permeate Flux and Salt Rejection).....	65
Figure 3.9.	Plain (Plain_0.0_Y_250) and Doped (C-Cu_0.8_Y_250) Membranes Performance Off-Sun at Different Feed Temperatures (Remaining Experimental Conditions Maintained at Standard Conditions) .....	66
Figure 3.10.	Plain (Plain_0.0_Y_250) and Doped (C-Cu_0.8_Y_250) Membranes Performance Off-Sun at Different Feed Flow Rates (Remaining Experimental Conditions Maintained at Standard Conditions) .....	67
Figure 3.11.	Plain (Plain_0.0_Y_250) and Doped (C-Cu_0.8_Y_250) Membranes Performance Off-Sun at Different Feed Concentrations (Remaining Experimental Conditions Maintained at Standard Conditions) .....	68

Figure 3.12.	Photothermal Effect on the Plain Membrane (Plain_0.0_Y_250) at Standard Conditions. Comparison of Off-Sun to On-Sun Performances (GHI of 582W/m <sup>2</sup> ) .....	69
Figure 3.13.	Summary of the Photothermal Effect on the Plain Membrane (Plain_0.0_Y_250) at Standard Conditions .....	70
Figure 3.14.	Photothermal Effect on the Doped Membrane (C-Cu_0.8_Y_250) at Standard Conditions. Comparison of Off-Sun to On-Sun Performances (GHI of 617 and 698 W/m <sup>2</sup> ) .....	71
Figure 3.15.	Summary of the Photothermal Effect on the Doped Membrane (C-Cu_0.8_Y_250) at Standard Conditions .....	71
Figure 3.16.	Summary of the Photothermal Effect on the Plain Membrane (Plain_0.0_Y_250) and the Doped Membrane (C-Cu_0.8_Y_250) at Standard Conditions.....	72
Figure 3.17.	Solar Module (CdTe_60%_225) Effect on the Photothermal Effect of the Doped Membrane (C-Cu_0.8_Y_250) at Standard Conditions. Membrane Performance Including and Excluding the Solar Module (GHI of 508 and 698 W/m <sup>2</sup> Respectively) .....	73
Figure 3.18.	Summary of the Solar Module (CdTe_60%_225) Effect on the Photothermal Effect of the Doped Membrane (C-Cu_0.8_Y_250) at Standard Conditions.....	74
Figure 3.19.	Desalination Performance Summary of the Proposed Hybrid PV-Membrane System at Standard Conditions. Plain membrane (Plain_0.0_Y_250), Doped membrane (C-Cu_0.8_Y_250), and Solar Module (CdTe_60%_225) .....	76

## LIST OF ABBREVIATIONS

AFM	Atomic Force Microscopy
AGMD	Air Gap Membrane Distillation
CA	Contact Angle
CB	Carbon Black
CFP	Capillary Flow Porometry
CNT	Carbon Nano-Tube
DCMD	Direct Contact Membrane Distillation
DI	Deionized
DIPS	Diffusion Induced Phase Separation
DLS	Dynamic Light Scattering
DMF	N,N-dimethylformamide
DRS	Diffuse Reflectance Spectra
DSC	Differential Scanning Calorimetry
ED	Electro Dialysis
EDS	Energy Dispersive X-ray Spectroscopy
FESEM	Field Emission Scanning Electron Microscopy
FF	Fill Factor
FTIR	Fourier Transform Infrared
GHI	Global Horizontal Irradiance
IDA	International Desalination Association

IR	Infrared
LED	Light Emitting Diode
LEP	Liquid Entry Pressure
LIPS	Liquid Induced Phase Separation
MD	Membrane Distillation
MED	Multi Effect Distillation
MEMD	Multi Effect Membrane Distillation
MF	Microfiltration
MGMD	Material Gap Membrane Distillation
MSF	Multi Stage Flash
NESMD	Nanophotonic Enabled Solar Membrane Distillation
NF	Nanofiltration
NP	Nanoparticle
NWS	Non-Woven Support
PA	Polyamide
PAN	Polyacrylonitrile
PC	Polycarbonate
PE	Polyethylene
PEEK	Polyether Ether Ketones
PEI	Polyetherimide
PES	Polyethersulfone
PI	Polyimide
PP	Polypropylene

PPT	Parts Per Thousand
PS	Polysulfone
PSD	Pore Size Distribution
PTFE	Polytetrafluoroethylene
PV	Photovoltaic
PVDF	Polyvinylidene Fluoride
RO	Reverse Osmosis
SEM	Scanning Electron Microscopy
SGMD	Sweep Gas Membrane Distillation
SHC	Solar Heating and Cooling
TEM	Transmission Emission Microscopy
TGA	Thermogravimetric Analysis
TIPS	Thermally Induced Phase Separation
TPC	Temperature Polarization Coefficient
UF	Ultrafiltration
UN	United Nations
UV	Ultraviolet
VIPS	Vapor Induced Phase Separation
VMD	Vacuum Membrane Distillation
VMEMD	Vacuum Multi Effect Membrane Distillation
XPS	X-ray Photoelectron Spectroscopy
XRD	X-ray Diffraction

## CHAPTER ONE: INTRODUCTION

### 1.1. The Need

The need for clean water has become one of the greatest challenges of the 21<sup>st</sup> century. The availability of this natural resource decreases over time as the demand keeps growing. Only 3% of the world's total water supply is fresh water, mainly located in ice and glaciers (~2.06%) and underground (~0.9%) [1]. Surface water (~0.03%), lakes and rivers, is the principal source for drinking, agricultural, and industrial purposes, but it only constitutes a small percentage of the total water capacity [2]. Currently, more than one billion people live with reduced access to fresh water, and the continuous growth in the world's population, industrialization, and climate change will only worsen the situation with time [1]. According to the United Nations (UN), more than 2 billion people are currently living with the risk of reduced access to fresh water resources [3].

Current data on population and water usage (domestic, agricultural, and industrial), in addition to the trends and forecast for the next decades, help us to predict the urgency for an alternative source for potable water. Water scarcity is becoming a critical threat to the population during this first half of the 21<sup>st</sup> century, specifically in developing countries with limited access to fresh water due to their arid location and lack of resources [4]. Malnutrition, diseases, and even death are the consequences for being deprived of this natural resource. On the other hand, saline water constitutes the remaining 97% of the world's total water, making it a huge potential solution to the

problem. Oceans, seas, and bays could be the reserve for the world's water consumption needs [2].

The United Nations predicts a 40% global water deficit by 2030 under a business as usual scenario, with the possibility of 2.3 billion people living in areas with severe water stress by 2050 [5]. Desalination of saline water through desalination processes seems to be a promising choice to satisfy the increasing need for potable water, containing less than 500 ppm of salt [6]. Multiple techniques currently exist, but the growing demand for clean water supplies is strongly driving the need to develop innovative, less energy intense, and environmentally friendly approaches to water desalination.

## **1.2. Motivation**

According to the International Desalination Association (IDA), water desalination is already practiced in 174 countries, providing potable water to more than 300 million people for some or all of their daily needs. These quantities translate to a total global cumulative desalination contracted capacity of 107 million m<sup>3</sup>/d [7]. Water desalination offers a wide spectrum of possibilities to produce clean water, making it attractive for research purposes. New desalination processes emerge occasionally, while continuous improvements and developments in existing processes are declared by their authors.

## **1.3. Introduction to Desalination**

Desalination is a purification process consisting of the extraction of dissolved mineral salts, organic substances, bacteria and viruses, and solids from saline waters to obtain fresh water [8]. There are many processes for desalination, and even nature uses it as the main source of fresh water. The vast majority of desalination processes use

membrane technology as the separation technique. The membrane acts as a physical barrier, separating a solution into two phases and allowing the transportation of specific compounds from one side to the other [8]. The portion that undergoes a phase change and travels through the membrane is the permeate flux, while the part that is rejected by the membrane is the retentate [1,9]. Figure 1.1 is a simple schematic of how membrane technology works.

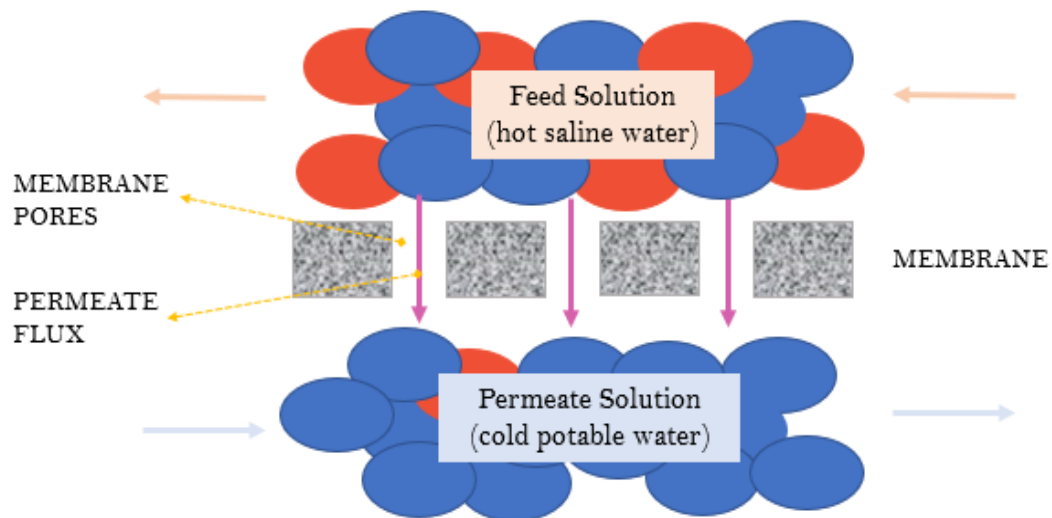


**Figure 1.1. Schematic Representation of Water Flux in Membrane Distillation [2,8]**

Membrane-based processes are prioritized due to its advantages, the knowledge already provided by research, and years of experience with multiple separation techniques. Since the first method used for desalination, the development of new techniques has been classified into three different categories: 1<sup>st</sup> generation or thermal-based techniques, 2<sup>nd</sup> generation or membrane-based techniques, and 3<sup>rd</sup> generation or hybrid techniques [1,6]. The 1<sup>st</sup> generation includes techniques such as multi-effect distillation (MED) or multi-stage flash (MSF), that imply phase changes during the

process. The 2<sup>nd</sup> generation includes techniques such as reverse osmosis (RO) or electro dialysis (ED), that involve membranes, but phase change is not necessary. Finally, the 3<sup>rd</sup> generation includes techniques such as membrane distillation (MD) or forward osmosis, that imply membranes and phase changes [1,2,4,6,10-14].

Currently, 60% of water desalination is produced through pressure driven processes, mainly through RO, ultrafiltration (UF), or nanofiltration (NF) techniques; while the remaining is produced by temperature driven processes, mainly through MED or MSF techniques [1]. There are drawbacks to both approaches, for example, limitations in the osmotic pressure in the first case or the high energy demand in the second [6]. A distinct approach for water desalination is offered by MD, which combines membrane and phase change systems [1,2,4,6,10-14].

MD has not been installed in new desalination plants, although it offers some advantages over the existing desalination processes [6]. Some of these advantages are: working with higher salinity levels due to a complete separation process; 100% theoretical rejection of non-volatile and dissolved substances, which indicates no wetting and less fouling; cost effectiveness due to lower operating parameters such as pressure and temperature [6]; and attractive for pairing with renewable energies such as solar or wind due to the low energy requirement [6,15].

#### **1.4. Introduction to Membrane Distillation (MD)**

Distillation is one type of water treatment process that involves the complete separation of vapor molecules from a liquid mixture via boiling, transportation of the vapor to a cooler location, saturation of the water vapor, and condensation into clean water [1,15,16]. Furthermore, membrane distillation is a thermally driven process in

which a microporous hydrophobic membrane acts as the physical barrier between the feed solution and the permeate solution. This thermal process only allows the separation of vapor molecules from the feed solution to pass through the membrane pores and condense on the permeate side. As the process is non-isothermal, the temperature difference existing between both solutions creates a temperature gradient through the liquid and vapor interfaces. This temperature gradient is responsible for the vapor pressure difference between the membrane surfaces, which is, ultimately, the driving force of the process [9,10].

MD has considerable advantages over the conventional distillation processes of RO, MED, or MSF. The feed solution is not required to boil, so lower operating temperatures are required. Therefore, the hydrostatic pressure required is lower and the process equipment is much smaller, making MD a more cost-effective process [2]. The reduced chemical interaction between the membrane and the feed solution requires less demanding membrane mechanical characteristics, and less expensive materials can be used in the manufacturing process. The membrane pore size required is relatively larger than other separation processes, such as RO, so less fouling occurs. Theoretically, MD is a complete separation process due to the vapor-liquid equilibrium, so a higher rejection factor is achieved [9]. Performance is not limited by the osmotic pressure or the concentration polarization, and higher salinity levels can be reached [10]. Moreover, MD systems have the flexibility to be combined with other separation processes, such as UF, NF, or RO, for highly purified permeates and are attractive to pair with low grade heat and renewable energy sources such as solar, wind, or geothermal for more ecological and cost-effective systems [6].

Although MD has many advantages, it also has some drawbacks that must be solved for optimum performance. These obstacles are membrane pore wetting, high conductive heat loss, and the temperature polarization phenomenon [4]. The main factors affecting membrane wetting are the surface tension of the feed solution, the membrane material, and the membrane structure [6]. These factors can be improved by using a membrane with a high water liquid entry pressure (LEP), which is achieved by using a membrane with high hydrophobicity and a small maximum pore size. Conductive heat loss can be reduced by utilizing a thick and highly porous membrane. The conductive heat transfer coefficient of the gas trapped inside the membrane is an order of magnitude smaller than the coefficient of the solid membrane material, so the porosity of the membrane is particularly important [12]. The temperature polarization phenomenon consists of the gradual decrease of temperature at the thermal boundary layers of the membrane due to the large amount of heat consumed and released in the process of phase transition, reducing the supply of heat for evaporation to the feed-membrane interface [17,18]. It is defined as the difference between the theoretical driving force and the actual driving force. The theoretical driving force is determined as the difference between the bulk feed temperature ( $T_{bf}$ ) and the bulk permeate temperature ( $T_{bp}$ ), while the actual driving force is determined as the temperature difference between the feed-membrane interface temperature ( $T_{mf}$ ) and the permeate-membrane interface temperature ( $T_{mp}$ ) [18,19]. Figure 1.2 is a simple schematic of the temperature polarization phenomenon.

The heat losses in MD can negatively affect the process by reducing the driving force up to 80% [19], leading to a drop in the flux across the membrane [6]. The mathematical expression of this phenomenon is the temperature polarization coefficient

(TPC), which is defined as the ratio between the actual driving force and the theoretical driving force and should be as close as possible to unity [18,19].

$$\text{TPC} = \frac{T_{mf} - T_{mp}}{T_{bf} - T_{bp}} \quad (1.1)$$

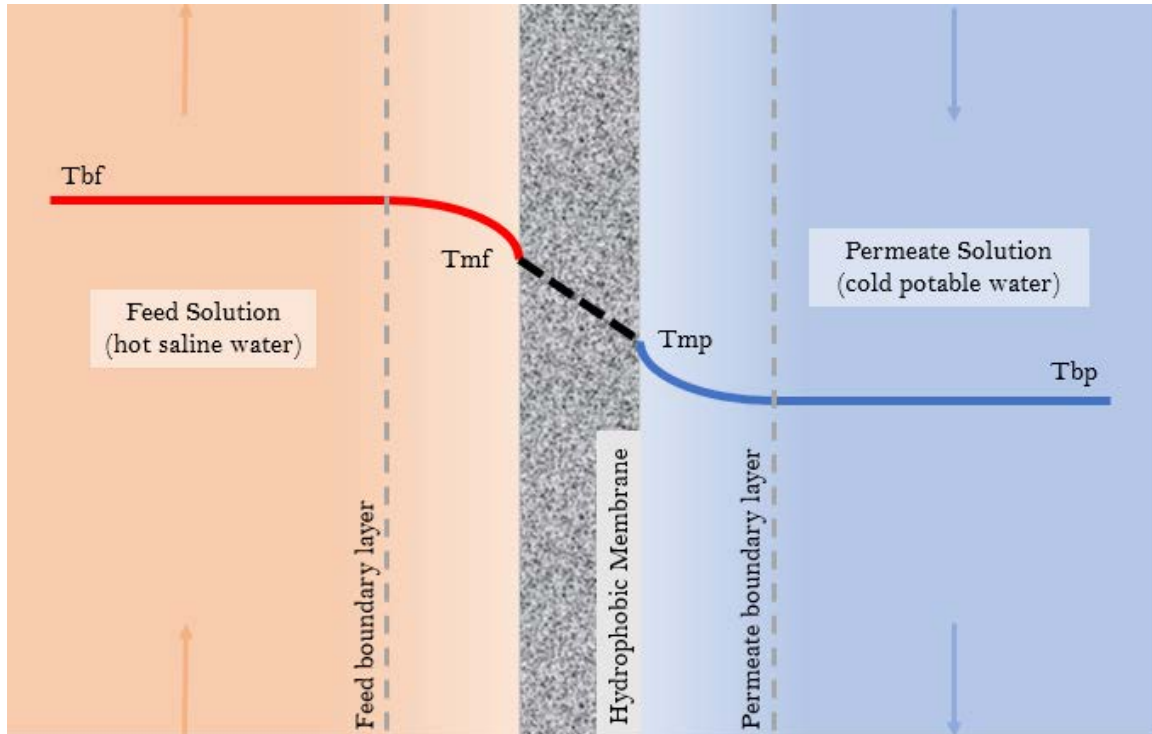


**Figure 1.2. Detailed Schematic Representation of the Temperature Polarization Phenomenon in MD [18,19]**

MD is mainly used for the distillation of brackish and seawaters at an affordable cost of 1.32 \$/m<sup>3</sup> [10]. Moreover, it can be used as a supplement or as an alternative to the conventional distillation processes [10]. However, the application field for this process is wide, and water recovery from wastewater streams is one of the most promising applications for the future [2]. Furthermore, other applications where MD has been used are: treatment of radioactive waste where the product could be safely discharged to the environment [9]; treatment of concentrated fruit juices and sugar solutions in the food industry; sterilization of biological fluids at high temperatures for

the medical industry; removal of organic and heavy metals from aqueous solutions in the environmental industry [6]; treatment of produced water after fracking containing very high levels of salts, various hydrocarbons and production chemicals in the oil and gas industry; temperature sensitive products such as pharmaceutical compounds, dairy products, natural aromatic compounds and solutions of several chemicals [1].

### **1.5. MD Configurations**

A number of different MD configurations are used for the desalination of brackish and seawater. Specifically, four configurations are the foundation for desalination: direct contact membrane distillation (DCMD), vacuum membrane distillation (VMD), air gap membrane distillation (AGMD), and sweep gas membrane distillation (SGMD) [2,6,9,10]. Figure 1.3 shows these configurations. However, extensive work has been done to develop new configurations and membrane modules that would include heat recovery and higher thermal efficiency such as: multi-stage and multi-effect membrane distillation (MEMD), vacuum multi-effect membrane distillation (VMEMD), hollow fiber MEMD, and material gap membrane distillation (MGMD) [14].

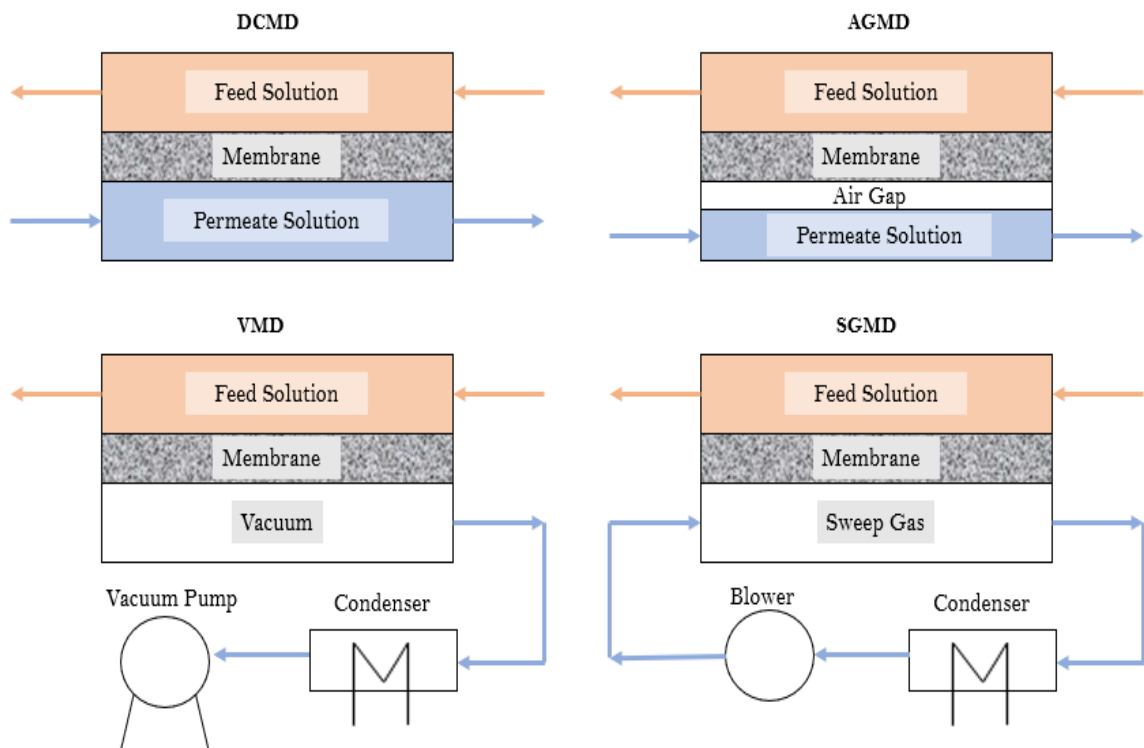


**Figure 1.3. Schematic Diagrams of Common MD Configurations: DCMD, AGMD, VMD, and SGMD [2,6,9,10]**

In the DCMD configuration, a hot saline aqueous solution is in direct contact with the feed side of the membrane, while a cold aqueous solution is in direct contact with the permeate side. The temperature difference across the membrane induces the vapor pressure difference responsible for the driving force of the system. Therefore, volatile molecules evaporate at the feed-membrane interface, move through the membrane pores by the pressure difference, and finally condense at the permeate membrane interface [14]. The hydrophobic characteristics of the membrane allow only a gas phase inside the membrane and avoid the penetration of the feed solution in the liquid state [9]. This configuration is characterized as the most popular and simplest configuration of MD, providing a high permeate flux, and the possibility of combining the MD with internal heat recovery. On the other hand, it is also characterized by its low thermal efficiency,

high heat conduction loss, and the high impact of temperature and concentration polarizations [2,4].

For the VMD configuration, the feed side remains the same, but the permeate side is modified. In this case, a vacuum pump applies a vacuum pressure on the membrane permeate side that transports the vapor to a condenser. Permeate condensation takes place outside the membrane module. It is important that the applied pressure is maintained below the saturation pressure of the volatile solvent in the feed solution [9,14]. This configuration is identified for its low heat conduction loss and high permeate flux. However, it is also characterized by a high membrane pore wetting, difficult heat recovery, and extra equipment required for condensation [2,4].

The AGMD configuration is very similar to DCMD, with differences only in the permeate side. The feed side is still a hot saline aqueous solution in direct contact with the membrane, but a thin stagnant air gap is introduced between the membrane and the condensation surface. In this case, the vapor travels across the membrane and the air gap to condensate over the cold surface inside the membrane cell [9,14]. This configuration is distinguished by its reduction of conduction heat loss, high thermal efficiency, possibility of using seawater as the cooling stream, and internal heat recovery. Conversely, the air gap creates additional mass transfer resistance, resulting in a lower permeate flux [2,4].

As for the SGMD, a cold inert gas sweeps through the permeate channel and collects vapor molecules from the membrane surface. The vapor is carried outside the membrane module to a condenser, where it condenses [9,14]. In this case, there is a gas barrier that reduces the conduction heat loss, as in AGMD, and enhances the mass transfer due to the continuous flow. Despite these advantageous characteristics, dealing

with a sweeping gas is intricate, and a small volume of permeate diffuses in a large volume of gas. This results in a large condenser being required and additional equipment costs [2,4].

New MD configurations have been developed based on the limitations and drawbacks of the four main methods. For example, the MEMD bases its design on an AGMD configuration with the addition of internal heat recovery for a reduction in energy consumption. A further step is the VMEMD configuration, which considers the MEMD design with the addition of vacuum. This enhancement aims to remove of excess air or vapor in the air gap region for a gain in the permeate flux. A similar concept is the hollow fiber MEMD, where a hollow fiber module is combined with an AGMD configuration and internal heat recovery. In the case of MGMD, the stagnant air used to fill the air gap in the AGMD configuration is replaced by different materials, such as polyurethane and polypropylene (PP) to enhance permeate flux [14].

## **1.6. Membrane Characteristics**

### Membrane Characteristics

The core of MD technology is the membrane, since it is the physical barrier between the retentate and the permeate. In order to be feasible, membranes need to meet some specific requirements such as: a hydrophobic layer in direct contact with the feed solution; high permeability, which is based on membrane thickness, porosity, pore size distribution, and tortuosity factor; made out of a material with low surface energy; good chemical, thermal, and physical resistance; high LEP; long term performance; and high heat transfer resistance but low mass transfer resistance [2]. Although all of these characteristics are important, several of them stand out for the desalination process.

The Liquid Entry Pressure (LEP), or sometimes called the wetting pressure, is one of the critical membrane characteristics for MD. It is the minimum hydrostatic pressure that must be applied onto the feed solution before it overcomes the hydrophobic forces of the membrane and penetrates into the membrane pores [1,6]. The LEP helps to prevent wetting of the membrane pores, which depend on the maximum pore size and the hydrophobicity. Also, the LEP is inversely proportional to the feed solution concentration [9]. The LEP equation has been proposed previously by Franken et al. [20].

$$\text{LEP} = P_f - P_p = \frac{-2 B \gamma_L \cos \theta}{r_{\max}} \quad (1.2)$$

Where  $P_f$  and  $P_p$  are the hydraulic pressure on the feed and permeate side,  $B$  is a geometric factor determined by pore structure with a value equal to 1 for cylindrical pores,  $\gamma_L$  is the liquid surface tension,  $\theta$  is the liquid/solid contact angle, and  $r_{\max}$  is the maximum pore size. A high LEP may be achieved using a membrane material with high hydrophobicity, high contact angle, a small maximum pore size, low surface energy, and high surface tension for the feed solution [1,4,9].

Hydrophobicity and hydrophilicity, defined as the ability to repel and absorb water respectively, are directly associated with the liquid/solid contact angle (CA). This angle quantifies the interaction of a liquid with a solid surface by measuring the relative degree between the liquid–gas tangent and membrane–liquid boundary [21]. Surfaces with a CA lower than 90 degrees are classified as hydrophilic, while surfaces equal to or greater than 90 degrees are considered hydrophobic [12]. See Figure 1.4 for CA characterization.

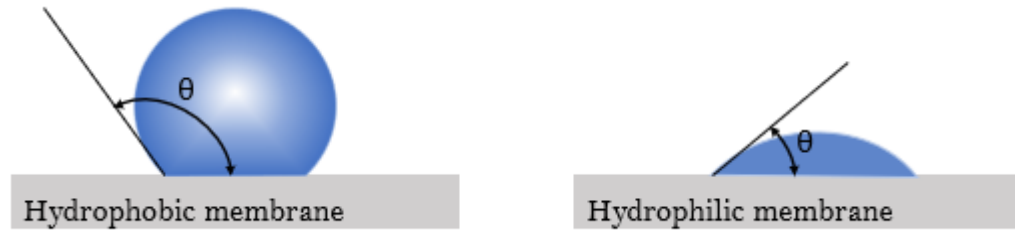


**Figure 1.4. Membrane Permeability Characterization by Contact Angle. Representation of Hydrophobic and Hydrophilic Surfaces [12]**

Membrane permeability is also a crucial characteristic of MD. It can be affected by a few specific factors, including membrane thickness, membrane porosity, pore size, and tortuosity [1,6]. Membrane thickness is responsible for the tradeoff between permeate flux and heat loss. As the thickness increases, both permeate flux and heat loss are reduced, forcing a compromise between both [4,9]. Membrane porosity is the most influential factor in the mass transfer rate across the membrane [4]. It refers to the void volume fraction of the membrane, or in other words, the volume of the pores divided by the total volume of the membrane. Higher porosity membranes have a larger evaporation surface area, which results in a higher permeate flux and lower conductive heat loss. The porosity ( $\varepsilon$ ) can be determined by Smolder–Franken's equation [22]:

$$\varepsilon = 1 - \frac{\rho_m}{\rho_{pol}} \quad (1.3)$$

where  $\rho_m$  is the density of the membrane and  $\rho_{pol}$  is the density of the polymer material.

Tortuosity ( $\tau$ ) is the deviation of the pore structure from the cylindrical shape. It influences the membrane permeability inversely, since the higher the tortuosity value, the lower the permeate flux [9]. The most successful correlation for tortuosity was introduced by Macki–Meares [23]:

$$\tau = \frac{(2-\varepsilon)^2}{\varepsilon} \quad (1.4)$$

Membranes frequently exhibit a pore size distribution (PSD) instead of a uniform pore size. This distribution should be as narrow as possible and is commonly in the range of 100 nm to 1 $\mu$ m [1]. An optimum PSD is required for each specific feed solution and operating condition due to its opposite effect in the permeate flux and wetting. Larger pore size results in higher permeate fluxes, but also increases the risk of liquid penetration [9].

**Table 1.1. PSD for Conventional Membrane Processes [8,21]**

Membrane Process	Micro Filtration (MF)	Membrane Distillation (MD)	Ultra Filtration (UF)	Nano Filtration (NF)	Reverse Osmosis (RO)
PSD (nm)	50-10,000	100-1,000	5-100	1-10	0.2-2

Thermal conductivity is the remaining essential membrane characteristic for MD. In this case, conduction heat loss occurs through the pores and the matrix of the membrane. Several possibilities arise to mitigate the heat loss, including membrane materials with low thermal conductivities, high porosity, and thicker membranes. The vast majority of hydrophobic polymers have heat conductivities of the same order of magnitude, so this option does not ensure improvement. The conductive heat transfer of the gas entrapped within the membrane pores is an order of magnitude smaller than the membrane matrix, making the gas the best possibility to reduce thermal conductivity, and thus, improve the permeate flux. As previously mentioned, membrane thickness requires a compromise due to the tradeoff of thickness over the mass transfer and heat transfer. Thinner membranes provide a higher mass transfer, while thicker membranes provide a lower conductive heat transfer [6]. Thermal conductivity is calculated based on the volume average of the polymer and gas thermal conductivities [9].

$$k_m = (1 - \varepsilon)k_s + \varepsilon k_g \quad (1.5)$$

Where  $k_s$  is the polymer thermal conductivity and  $k_g$  is the gas thermal conductivity. Even so, another method exists to calculate thermal conductivity based on the volume average of both resistances ( $1/k_s$  and  $1/k_g$ ). Polymer and gas thermal conductivities depend on temperature and are calculated using the equations (1.6) and (1.7), respectively [9].

$$k_s = 4.86 \times 10^{-4} T + 0.253 \quad (1.6)$$

$$k_g = 1.5 \times 10^{-3} \sqrt{T} \quad (1.7)$$

### Membrane Materials

The hydrophobic forces of the membrane are an important requirement for MD. In most applications, hydrophobic materials with low surface energy are used to ensure proper performance. Originally, materials such as silicone coated glass fibers or nylon were investigated with unsuccessful wetting resistance [14]. Currently, hydrophobic polymers are commonly used to establish the passage of vapor only across the membrane pores while retaining the liquid. Polytetrafluoroethylene (PTFE), polyvinylidene fluoride (PVDF), polypropylene (PP), and polyethylene (PE) are the most universal of those polymers [14]. PVDF is the most popular due to its easy processability, its thermal, and its chemical resistance. PTFE exhibits the best hydrophobic characteristics, but it is not soluble in many solvents, making it difficult to process [1]. Other polymers widely used for commercial membranes are cellulose acetate, polysulfone (PS), polyethersulfone (PES), polyacrylonitrile (PAN), polyetherimide (PEI), polycarbonate (PC), polyamide (PA), polyimide (PI), and polyether ether ketones (PEEK) [8].

**Table 1.2. Properties of Polymer Materials [4,14]**

<b>Polymer Material</b>	<b>Surface Energy (<math>\times 10^{-3} \text{ N m}^{-1}</math>)</b>	<b>Thermal Conductivity (<math>\text{W m}^{-1} \text{ K}^{-1}</math>)</b>	<b>Thermal Stability</b>	<b>Chemical Stability</b>
PTFE	9 - 20	0.25	High	High
PVDF	30.3	0.19	Medium	High
PP	30	0.17	Medium	High
PE	28 – 33.2	0.40	Low	High

### Membrane Characterization Techniques

Many techniques are required to characterize the wide range of membrane properties. Physical, mechanical, chemical, and optical properties can be found among them. In most cases, multiple techniques can be used to characterize the same property with some technical differences between them.

A number of techniques to characterize the surface and cross section morphology are available, including scanning electron microscopy (SEM), field emission SEM (FE-SEM), transmission emission microscopy (TEM), and atomic force microscopy (AFM) [12,24-26]. In the SEM case, a thin coating of gold, palladium, chromium, or carbon is sputtered onto the samples before imaging to avoid charging [12]. This technique is commonly used to obtain the pore size and the thickness of the membranes. AFM can be used to characterize the pore size distribution (PSD), topography, and surface roughness of the membranes [24]. In addition, another technique used to measure PSD is capillary flow porometry (CFP) [25].

An important property of membranes, contact angle (CA), can be characterized by using a goniometer or an optical tensiometer equipped with an imaging processing software. A small volume of deionized (DI) water is dropped on top of the membrane

surface for measurement [12,24]. Furthermore, the gravimetric method can calculate the membrane porosity or the membrane void volume fraction. This method uses dry and saturated samples in ethanol to calculate the membrane porosity. On a different note, mechanical properties such as the tensile strength and the strain can be identified by tensile tests using a universal test machine [24].

Another influential property of membranes, LEP, can be characterized by using a dead-end cell, DI water, and compressed nitrogen. The pressure is recorded for determination of the LEP value [27].

Multiple techniques characterize the chemical composition: X-ray photoelectron spectroscopy (XPS), Fourier transform infrared (FTIR), and energy dispersive X-ray spectroscopy (EDS) [24,27-29]. Moreover, to determine the membrane's relative degree of crystallinity and the crystalline structure of the polymers, techniques such as X-ray-diffraction (XRD) and differential scanning calorimetry (DSC) are available [12,25].

The thermal stability is characterized by multiple techniques, including thermogravimetric analysis (TGA) and DSC [30]. The optical properties are characterized by diffuse reflectance spectra (DRS) using a spectrophotometer, and dynamic light scattering (DLS) analysis [26].

#### Membrane Fabrication Processes and Geometries

Generally, membranes are fabricated in two types of geometries: flat sheet and hollow fiber. Their geometry depends on the fabrication method used, which is usually selected based on a specific application. A number of different methods are available to fabricate membranes. The most popular and commercially used techniques are phase

inversion and spinning, but other techniques can also be used, such as sintering, stretching, or template leaching [8].

During a phase inversion technique, a polymer solution transforms from the liquid to the solid phase in a controlled procedure. The morphology of the membrane is controlled in the initial stage of the phase transition [21]. During the precipitation step, the difference between the surface and the interfacial tension of the cast-film and air, and the cast-film and water, respectively, force the polymer molecules at the top of the cast film downwards into the bulk of the film. The polymer chains cannot easily move downward from the interface due to their long chain nature, leading to flattening and characterizing their geometry [12]. Multiple techniques belonging to the phase inversion category are classified according to the separation mechanism involved. Two mechanisms exist due to the change of the operating parameters that induce the phase inversion [8].

The first mechanism is thermally induced phase separation (TIPS), which consists of the precipitation of the polymer solution by its temperature decrease due to the decrease in solvent quality [21]. The second mechanism is diffusion induced phase separation (DIPS), which consists of the precipitation of the polymer solution by contacting it to a vapor or liquid. Diffusional mass exchange is responsible for the change in the local composition of the polymer film.

Three different techniques are classified under DIPS [8]. The first technique, immersion precipitation, where the polymer solution is immersed into a non-solvent coagulation bath, typically water, and the non-solvent from the bath diffuses into the polymer solution. The solvent diffuses from the polymer solution to the non-solvent bath,

causing a rapid precipitation from the top surface to the bottom of the polymer solution. The second technique, vapor absorption, where the polymer solution is exposed to a vapor containing non-solvent, typically water, and some gases such as air or nitrogen. The absorption of the non-solvent causes the polymer solution precipitation. The third technique, solvent evaporation, where the polymer solution is prepared with a polymer, a volatile solvent, and a non-volatile non-solvent. Evaporation of the solvent causes unstable compositions, which leads to the polymer solution precipitation [8,21].

During a spinning technique, the polymer solution passes through a spinneret with a precision orifice containing a centrally positioned inlet tube for the delivery of the internal coagulation medium. The hollow fibers must be viscous enough to support the virgin fiber. The spinneret can be placed for wet spinning, dry-wet spinning, or dry spinning configurations. The spinning conditions influence the membrane shape and morphology, and thus, the overall performance. The solvent / non-solvent ratio of the internal bore liquid determines the pore structure at the inner surface, while the air gap conditions determine the pore structure at the outer surface [8]. Electrospinning represents the most used possibility of this technique, which consists of applying a high potential between the polymer solution and a grounded rotating collector. When the electrostatic potential overcomes the surface tension of the droplet, a charged liquid jet forms, which elongates and travels through the air to reach the collector, where it solidifies in the form of nanofibers [21,24].

### **1.7. Solar Assisted MD Background**

Solar assisted MD has been broadly examined to deliver the thermal and electrical energy required to run the desalination process. Using solar photovoltaic cells to provide

the electrical power and solar collectors to provide the thermal energy are configurations commonly used in solar technologies coupled with membrane distillation [6]. The cost associated with these technologies can range from 8.9 \$/m<sup>3</sup> to 18 \$/m<sup>3</sup>, where the membrane and plant lifetime are the key parameters [6]. An example of solar assisted MD is the MEDESOL project, which assesses a cost effective and high efficiency multistage membrane distillation concept. The solar multistage MD system involves the integration of multiple membrane distillation modules coupled to a solar concentrator for thermal energy [31]. More solar assisted MD projects are summarized by Mahdi et al. in their membrane distillation review [2]. During this review, a total of six systems coupled with thermal or electrical energy sources are organized chronologically.

However, an analysis of a potential combination of photovoltaic (PV) or thermal with desalination in a hybrid system or directly heating the membrane with solar energy is difficult to find. Calise et al. presented novel work by developing a polygeneration system consisting of a concentrating PV/Thermal collector, solar heating and cooling (SHC), and MED [32]. Their numerical case study reveals the potential energy saving this type of system provides. Summers et al. patented an AGMD system, which includes a dyed solar absorbing membrane positioned to receive solar radiation as the thermal input [33]. Dongare et al. demonstrated photothermal heating induced by solar irradiance in a nanophotonic enabled solar membrane distillation (NESMD) configuration [16]. An optical absorbing coating layer on top of the membrane was capable of producing enough localized photothermal heating to drive the distillation process and thus, eliminate the requirement of heating the input water.

The temperature polarization phenomenon and its effect on water flux has also been widely investigated by simulation models as well as experimental methods. Temperature polarization can be mitigated using hydrophobic microporous membranes with high permeability due to a total pressure gradient [18]. This phenomenon is dependent on multiple operational parameters such as velocity, concentration, temperature, and the use of spacers. The use of flow promoters, or spacers, with different thicknesses and geometries improves the temperature polarization coefficient [17,19]. Moreover, velocity and concentration are directly proportional to TPC, while temperature is inversely proportional [34]. Other studies focus on simulating the heat and mass transfer across the membrane to predict the flux and temperature polarization coefficient [19,35,36].

An innovative approach to influence the temperature polarization was introduced by Vanherck et al. via plasmonic heating [26]. They demonstrated an increase of flux by incorporating gold nanoparticles (NPs) into the membrane and irradiating the membrane with laser light close to the surface plasmon resonance wavelength of the NPs. The nanoparticles experience plasmonic heating when they are exposed to wavelengths of light corresponding to the plasmon resonance and thus, they are capable of converting light into heat energy efficiently [26,37]. To guarantee a high light-to-heat conversion efficiency, NPs with significant absorption efficiencies and poor luminescence quantum yields are necessary [38]. Further work with gold nanoparticles and laser irradiance illustrates the concept of localized thermal heating [39].

The study of photothermal heating has been extended to other type of nanoparticles and light sources. Li et al. replaced gold NPs and laser radiation with silver

NPs and Light Emitting Diode (LED) light. They proved that this combination is a good alternative to the previous study regarding performance and cost [40]. Politano et al. reviewed membrane processes involving the photothermal effect under light irradiance and hypothesized the possible reasons for permeability enhancement. They concretely focused on solvent heat capacity, amount of NPs incorporated in the membrane, laser intensity, and transmembrane flow rate as the influential factors for improvement [38]. In further studies, they demonstrated the potential of plasmonic heating by irradiating ultraviolet (UV) light to membranes incorporating silver nanoparticles. They demonstrated an increase in flux and bulk membrane temperatures with increased nanoparticle loading [15,41].

More recently, carbon black nanoparticles have been employed for plasmonic heating [16,42]. Dongare et al. coated a layer of carbon black NPs over an existing membrane and induced highly localized photothermal heating by solar illumination to drive the distillation process [16]. Similarly, Lind et al. exposed a coated membrane to simulated solar irradiance to enhance the desalination permeate flux [42].

The tunability of plasmonics has recently emerged as a new route to enhance the photothermal effect by the colloidal synthesis of nanostructures. Dopant distribution presents a new frontier of opportunity for tunable plasmonic materials [43]. Extensive work has been done to prove the concept of photothermal heating and its possible enhancement. Pioneer work regarding nanoshells was done by Oldenburg et al. after they revealed that the optical resonance of a metal nanoshell, a dielectric core, and a metallic shell can be modified in a controlled fashion. By varying the core and shell dimensions, they demonstrated the wavelength optical resonance shift over hundreds of nanometers

[44]. Moreover, Halas verified that nanoshell geometry is ideal for tuning and optimizing the surface plasmon resonance [45]. Further investigation by Knight and Halas showed the near and far field properties of few nanoshell versions [46]. Along the same lines, Yu et al. observed a dominant surface plasma band corresponding to the longitudinal resonance in the absorption spectral of gold nanorods. Also, the maximum wavelength red-shifted, which is an increase in wavelength in proportion to the aspect ratio [47]. Additionally, Jain et al. calculated the optical properties of gold nanoparticles of different sizes, shapes, compositions, and aggregation by using the Mie theory and discrete dipole approximation [48].

The addition of nanoparticles is also demonstrated to have an impact on membrane performance [24,49]. Roshani et al. showed evidence that the addition of polystyrene/ZnO (PS/ZnO) caused an increase in porosity, surface roughness, and contact angle, which ultimately resulted in a significant increase in membrane performance [49]. Similarly, Tijing et al. fabricated superhydrophobic membranes by coating a layer of carbon nanotubes on top of a nanofiber membrane to enhance the hydrophobicity of the membrane, and therefore the permeate flux [24].

**Table 1.3. Summary of Previous Solar Assisted MD Performance When the Membrane is Directly Exposed to Irradiance**

Article Author	MD Configuration	Light Source	NP Type	Energy System	Water Flux (L/m <sup>2</sup> h)	Light Flux (W/m <sup>2</sup> )
Dongare et al. [16]	NESMD	Sunlight	Carbon Black (CB)	None	1.12	0
					2.72	700
Vanherck et al. [26]	Dead-end filtration	Laser	Gold	None	9.35	0
					11.9	2000
Vanherck et al. [37]	Dead-end filtration	Laser	Gold	None	1.5	0
					1.75	2000
Li et al. [39]	Dead-end filtration	Argon laser	Gold	None	0.7	0
					0.9	5000
Li et al. [40]	Dead-end filtration	LED	Silver	None	1.1	0
					1.2	0.21
Politano et al. [41]	VMD	UV lamp	Silver	None	3	0
					25.7	2.3e10 <sup>4</sup>
Lind [42]	Pervaporation	Xenon lamp	Carbon Black (CB)	None	1.2	0
					1.9	23000

In conclusion, while these works have demonstrated the potential for coupling MD with solar systems and the use of photothermal heating to reduce the energy required and improve the permeate flux, there is still little analysis of the potential combination of PV/thermal with desalination in a hybrid system or of directly heating the membrane with solar energy. Further fundamental understanding is still necessary, as well as the integration of MD into a working prototype involving a natural light source. This need leads to the proposal of a new design that will combine a solar photovoltaic cell with a

spectrally selective nanoparticle doped membrane to develop a hybrid system capable of co-producing electricity and clean distillate. Furthermore, contributing to advance the state-of-the-art of MD.

### **1.8. Study Scope and Objectives**

The opportunity identified in the previous sections results in the disclosure of a new study to provide awareness of a system capable of supplying electrical energy and clean distillate, while overcoming distillation drawbacks such as temperature polarization and conduction heat losses. A DCMD configuration is selected among all MD configurations, as well as a photovoltaic module, due to the building simplicity of the system for research purposes.

The proposed design considers the advantages of MD by combining DCMD with a photovoltaic (PV) cell. This hybrid design consists of a membrane distillation system with a PV cell incorporated on top of the direct contact membrane module. As the first layer of the design, the PV cell collects a portion of the visible solar spectrum while allowing the remaining energy to pass through and reach the membrane module. Next, the filtered solar energy travels through a second layer, the feed stream, helping to warm the stream and lower the system energy requirements. Then, the energy reaches the membrane, a third and final layer of the design, at the core of the module, where it can be absorbed, reflected, or transmitted. In order to absorb most of the energy reaching the membrane, NPs of different chemical compositions can be doped into the membrane. This process helps to mitigate the temperature polarization effect and the conduction losses, principal disadvantages of DCMD, and therefore to improve the permeate flux of the system. Figure 1.5 exhibits the proposed design.

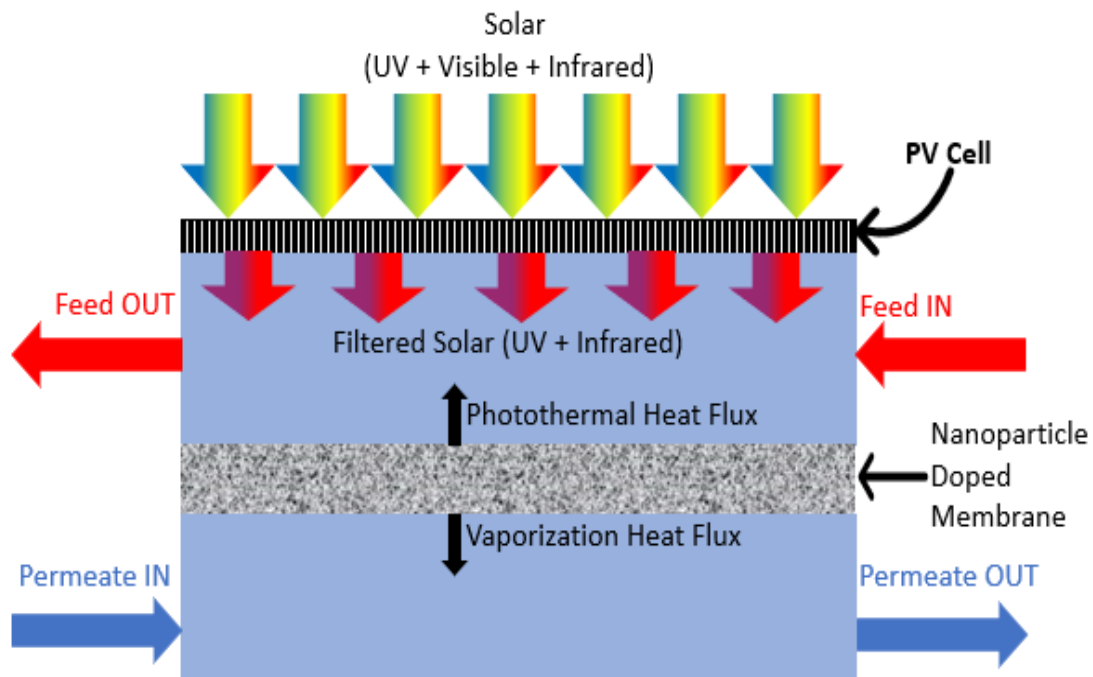


**Figure 1.5. Proposed Hybrid PV-Membrane System Design**

This hybrid design has been previously simulated to prove its potential. Otanicar et al. developed a theoretical model to investigate the role of the solar concentration level, and the lower wavelength of the spectral filtration on both the water flux and the electrical production from the PV cell [50]. This work focuses on the development of an experimental test bed capable of demonstrating the proposed concept and validating the model.

This study consists of two high level objectives: the synthesis and characterization of selectively absorbing nanoparticle doped membranes presented in chapter 2 and, the design and characterization of a hybrid membrane distillations and photovoltaic cell system presented in chapter 3.

Chapter 2 focuses on developing a membrane synthesis process capable of incorporating nanoparticles and the characterization of the membranes fabricated. The

synthesis process must result in a microporous hydrophobic membrane with a uniform distribution of NPs across the membrane volume and with a contact angle equal to or higher than 90 degrees [12]. Moreover, the nanoparticles doped into the membrane must be capable of enhancing the energy absorption for wavelengths across the whole solar spectrum. Finally, a desalination characterization of the fabricated membranes is necessary. The nanoparticle doped membrane must exhibit an improvement in permeate flux under solar irradiance with respect to an undoped membrane [15,40]. The uniform nanoparticle incorporation into the membrane must impact the temperature polarization effect and the permeate flux. A test apparatus is required for the membrane desalination characterization, which is associated with the second high level objective of the project.

Chapter 3 focuses on the design, construction, and performance characterization of a hybrid MD with a PV cell prototype incorporating the proposed membrane module. The experimental system must include two closed loops, the feed and the permeate streams, capable of providing the necessary testing conditions on each side, and a data acquisition system for data logging. Moreover, the characterization off-sun and on-sun of the hybrid system is required. The system must be able to co-produce electrical energy and clean distillate while mapping the system performance at different testing conditions. Specifically, the system with a nanoparticle doped membrane must be able to distill water at a higher rate than the system using an undoped membrane, proving the enhancement of the temperature polarization effect and the permeate flux due to the nanoparticle localized photothermal heating. In order to verify the effect of the hybrid design, including NPs in the membrane and a PV cell on top of the membrane module, a set of tests are required to be run indoors and outdoors for direct comparison. Experimental testing will cover

multiple feed and permeate temperatures, feed and permeate flow rates, and feed salinity levels.

## CHAPTER TWO: MEMBRANE SYNTHESIS AND CHARACTERIZATION

This chapter focuses on the first high level objective of the study, the development of a membrane synthesis process capable of incorporating nanoparticles and the optical and morphological characterization of the membranes fabricated.

### 2.1. Materials

Hydrophobic polymers are commonly selected for the synthesis of MD membranes due to their characteristics of easy fabrication, modification, scale-up, and low cost [14]. PVDF is selected in this case as the base polymer for the membrane synthesis due to its easy processability, thermal stability, hydrophobicity, mechanical strength, and resistance to corrosive chemicals characteristics [21,25,51]. This semi-crystalline polymer contains a crystalline phase, which provides thermal stability, and an amorphous phase, which provides flexibility towards membrane applications [14]. Moreover, the affinity between the solvent and the polymer is the most influential parameter in the membrane permeate flux [52]. N,N-dimethylformamide (DMF) is selected in this case as the base solvent for an easy dissolution with the base polymer and quick precipitation during the immersion process [21].

Materials used in traditional membranes do not exhibit high solar absorption [15]. However, nanoparticles are an attractive solution for modifying the optical properties of the membrane due to their high absorption characteristics at low particle loadings [44,45,53,54]. Noble metal nanoparticles are specifically excellent absorbers of visible

light due to their surface plasmon resonance characteristics [48]. One of the most significantly researched morphologies is the silica-gold core-shell structure, which has highly tunable spectral properties by adjusting the shell thickness relative to the core diameter [46,48]. Although any nanoparticle can enhance the absorption of a membrane, nanoparticles with high absorption characteristics such as carbon nanotubes or graphite are desirable for this application [55].

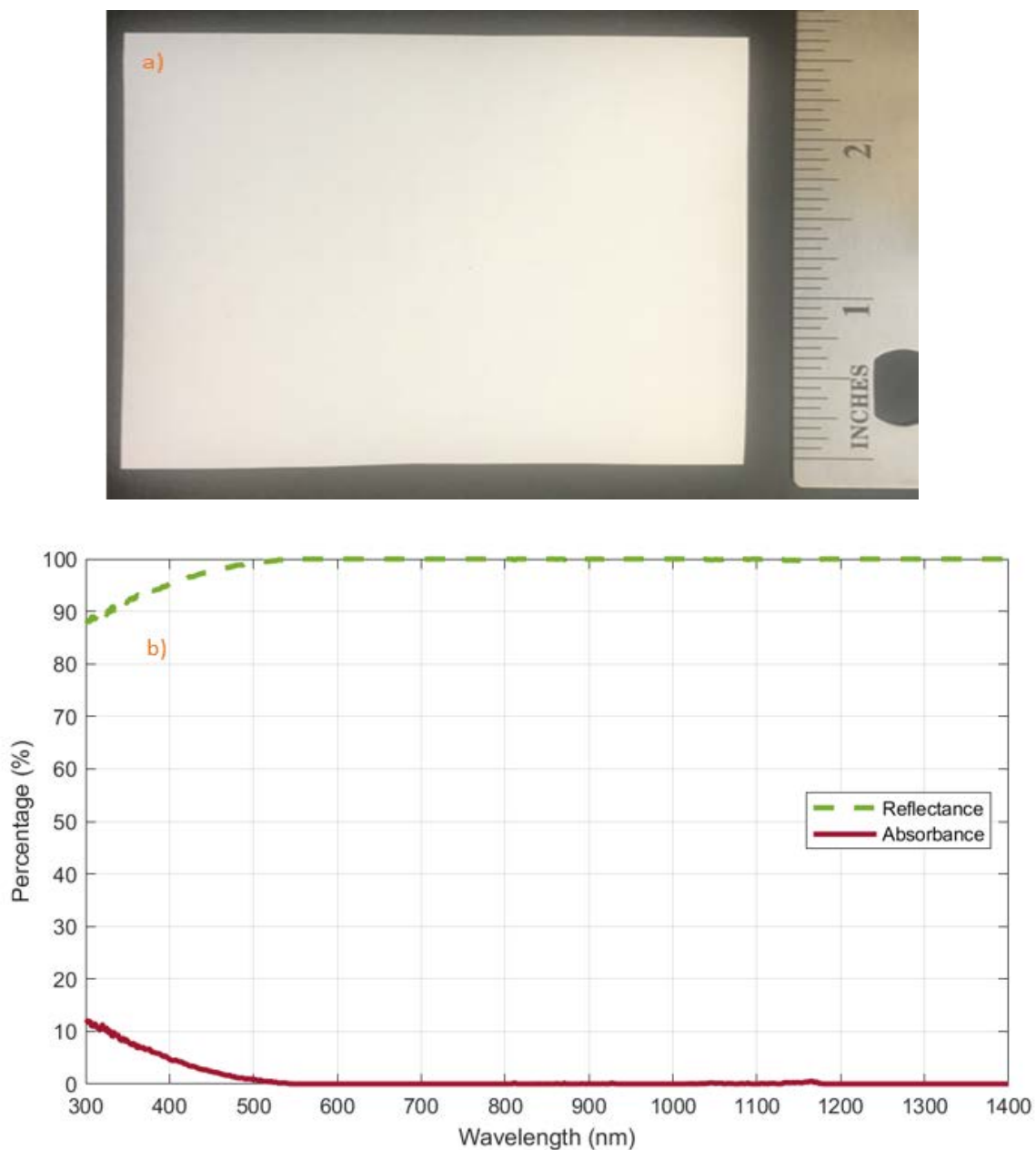


**Figure 2.1. Commercial PVDF Membrane: a) Physical Sample, b) Spectral Optical Properties**

The base solution for the membranes used in this study is made out of PVDF (HSV900, >99% by wt., kindly provided by Arkema) as the polymer, and N,N-dimethylformamide (DMF, DX1730, Sigma Aldrich) as the solvent. The nanoparticles considered for doping purposes of the base solution are carbon coated copper nanopowder (Cu, carbon coated, 99.8%, 25 nm, Nanoamor), silver nanopowder (Ag,

99.95%, 100nm, SkySpring Nanomaterials, Inc.), and gold coated silica nanoshells (Au SiO<sub>2</sub>, 85nm, nanoComposix). The hydrophobic membranes fabricated with only the base solution are considered plain PVDF membranes, while the membranes containing nanoparticles are considered doped membranes. The nomenclature for plain and doped membranes fabricated during this study is the following: “NP type\_NP weight percent (wt%)\_Addition of support (Y/N)\_Casting membrane thickness (μm)”.

## 2.2. Membrane Synthesis

Phase inversion is a commonly used technique for the fabrication of membranes in previous works. The process can be used for the fabrication of plain membranes as in the Khayet et al. study [56], or it can be altered by adding additives or nanoparticles to investigate the effect on morphology and transport properties. For example, Fontananova et al. and Bilad et al. developed phase inversion processes that included additives such as LiCl in the casting solution. They were capable of reducing macrovoid formation and increasing the mechanical stability of the membranes [51,57]. Similarly, Roshani et al. developed a novel nanocomposite membrane by including a concentration of ZnO during the phase inversion process. The addition of ZnO NPs increased the pore size and therefore, the membrane porosity [49]. Photothermal plasmonic heating to improve the MD performance was achieved by adding Ag NPs in the case of Politano et al. [15,41] and adding Au NPs in the case of Vanherck et al. [26]. Contact angle enhancement is another reason for the addition of additives, as shown by Wei et al. with TiO<sub>2</sub> nanowires [58].

An important factor during the phase inversion process for non-supported membranes is shrinkage. Although there is little information in the literature, Bilad et al.

addressed the relevance of this phenomenon [51]. The polymer is subjected to an action force after a film is casted, which draws the polymer towards the center of the film, causing shrinkage. This force is due to a difference in surface tension between the film casted and the air before the coagulation bath, and between the film and the water during the bath. This phenomenon is commonly solved using non-woven supports (NWS), which provide enough mechanical strength to overcome the shrinkage force [51]. They also reported a shrinkage increase as the casting thickness and the polymer concentration increases.

Different fabrication processes can be used for membrane synthesis, but the casting solution suffers little changes for every process. Electrospinning is another commonly used technique for the fabrication of PVDF membranes, as in Lalia et al [21]. Moreover, Dongare et al. also used this technique to coat a Carbon Black (CB) layer on top of a PVDF membrane to obtain a photothermal plasmonic effect [16]. Contact angle and performance enhancements were proved via the addition of TiO<sub>2</sub> NPs by Lee et al. [29], clay nanocomposite by Prince et al. [27], and Carbon Nanotubes (CNTs) by Tijing et al [24]. Vapor Induced Phase Separation (VIPS) and Liquid Induced Phase Separation (LIPS) are more recent processes, as shown by AlMarzooqi et al. [12] and Meringolo et al [59].

A custom phase inversion process fabricates the plain membranes synthesized during this study. An immersion precipitation is specifically selected for a diffusion induced phase separation (DIPS) process due to the simplicity of the process for research purposes. First, 89 wt.% of solvent (DMF) is added into a jar and placed on a magnetic stirrer (MR HEI-standard Heidolph). Then, 11 wt.% of polymer (PVDF) is added

gradually to the jar to mix the components at ambient temperature and 150 rpm for 24 hours. The mixed solution is placed in a standard chamber connected to a vacuum pump (DV-4E-250 eliminator) for de-gas during at least 2 hours or until all bubbles are released. Next, the solution is casted over a non-woven support (Novatexx 2483, kindly provided by Freudenberg) by using an adjustable doctor blade with an automatic film coater (MTI corporation MSK-AFA-II) at a speed of 10 mm/sec and a casting thickness of 250  $\mu\text{m}$  [6,51]. The membrane is quickly immersed into a non-solvent coagulation bath containing DI water at room temperature for immersion precipitation and maintained for 24 hours to remove any solvent residue. Finally, the membrane is dried in an oven at 60°C for 24 hours to evaporate all traces of solvent and complete cross-linking [49,52,57].

The doped membranes synthesized in this study result from the combination between ultrasonication and the phase inversion process above. Ultrasonication is necessary as a pre-step for the adequate dispersion of the nanoparticles in the solvent. First, 89 wt.% of solvent and 0.8 wt.% of NPs (25 nm of copper (Cu) carbon coated) are added into a jar and placed inside a chamber for ultrasonication (Q500 sonicator) during 15 minutes at 50/10 seconds intervals and 30% amplitude [15]. Following ultrasonication, the mixture is placed on a magnetic stirrer, where 10.2 wt.% of polymer is added gradually. The subsequent steps replicate the phase inversion process used for the synthesis of plain membranes.

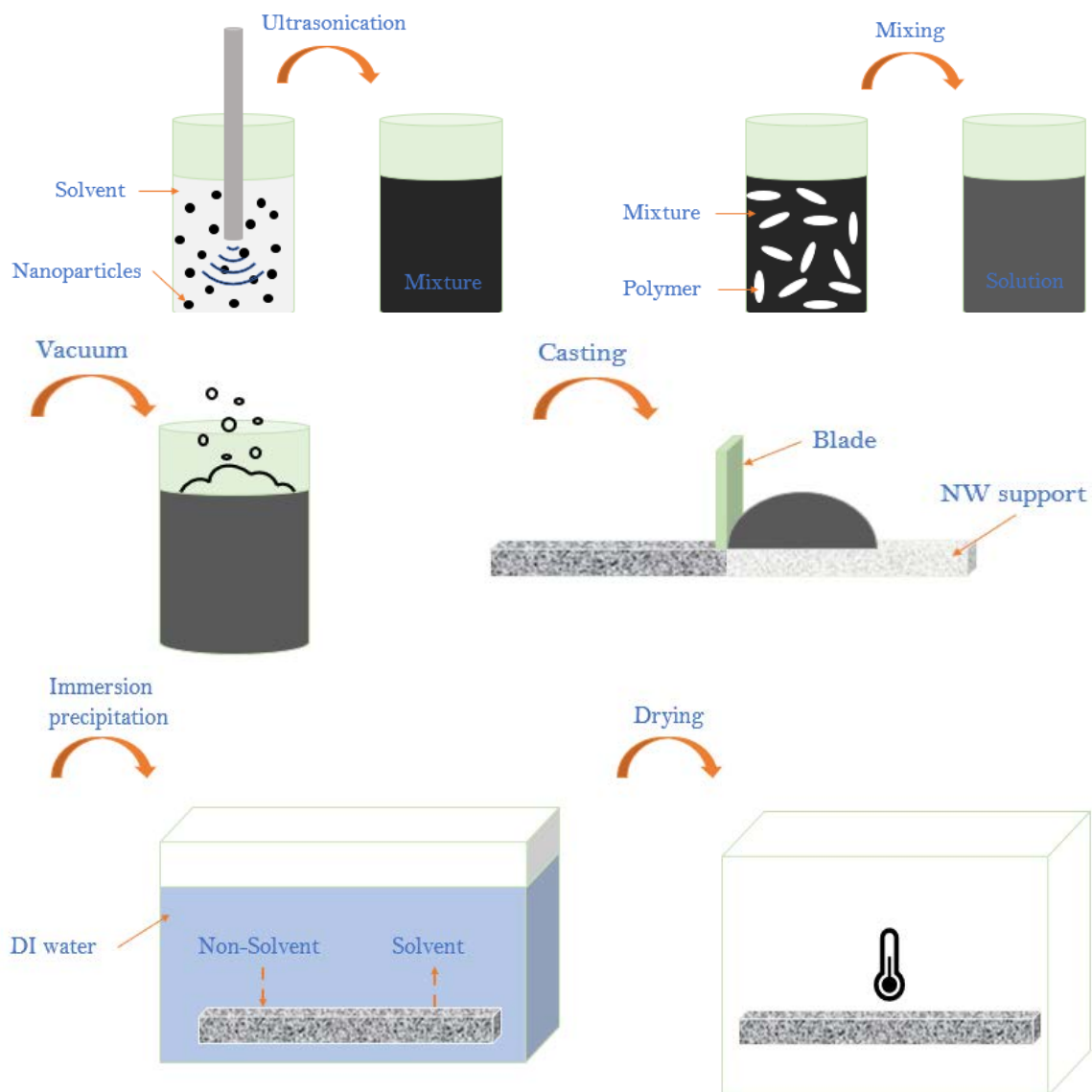


**Figure 2.2. Schematic of Custom Phase Inversion Process**

Figure 2.3 displays the final membranes, plain and doped, produced by the developed phase inversion process, and used for performance characterization. Table 2.1 summarizes the composition of the different membranes fabricated during this study. The plain and doped membranes are employed to accomplish the project's objectives, while the remaining membranes are trials used in a preliminary analysis to determine the best possible nanoparticle doping option.

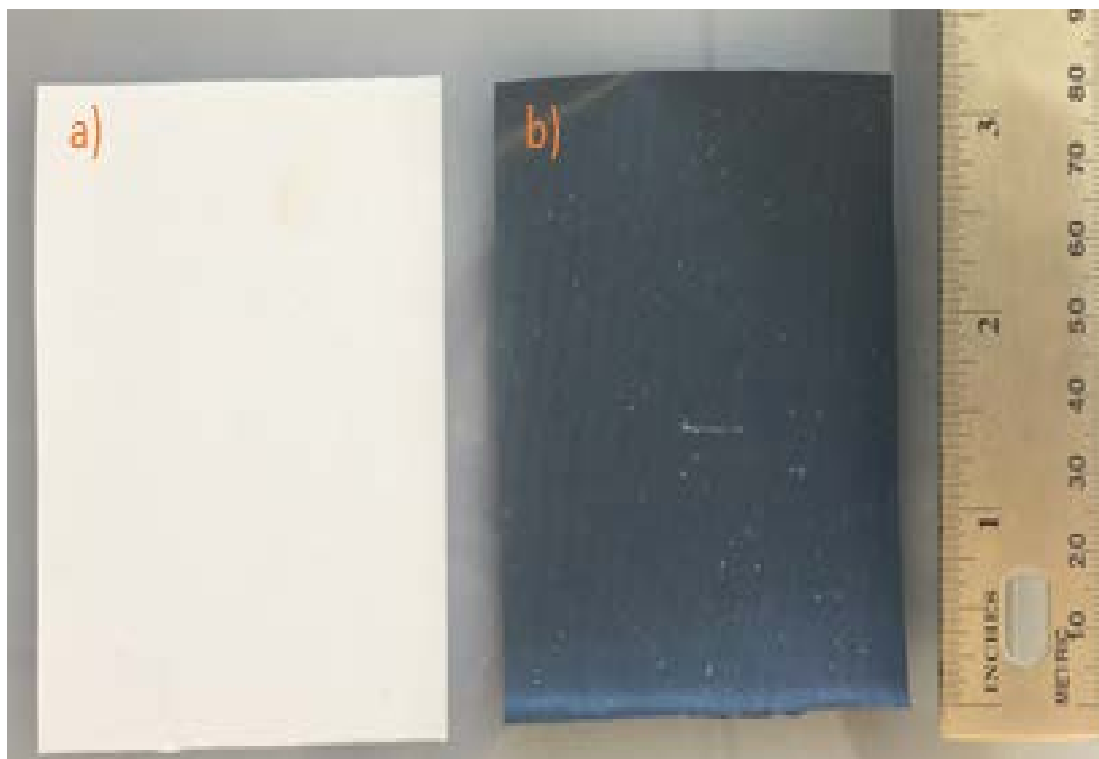


**Figure 2.3. Membranes Fabricated by Custom Phase Inversion Process: a) Plain (Plain\_0.0\_Y\_250), b) Doped (C-Cu\_0.8\_Y\_250)**

**Table 2.1. Summary of Membrane Fabrication Parameters**

Membrane Name	NWS Type	Casting Thickness ( $\mu\text{m}$ )	PVDF (wt%)	DMF (wt%)	NP Type	NP (wt%)
<i>Plain_0.0_Y_250</i> (“Plain Membrane”)	Novatexx 2483	250	11.0	89.0	None	0.0
<i>C-Cu_0.8_Y_250</i> (“Doped Membrane”)	Novatexx 2483	250	10.2	89.0	C-Cu	0.8
<i>Plain_0.0_N_120</i>	None	120	16.0	84.0	None	0.0
<i>Au-SiO<sub>2</sub>_0.8_N_120</i>	None	120	15.6	83.6	Au-SiO <sub>2</sub>	0.8
<i>Ag_0.8_N_120</i>	None	120	15.6	83.6	Ag	0.8
<i>C-Cu_0.8_N_120</i>	None	120	15.6	83.6	C-Cu	0.8

### 2.3. Optical Characterization

The membranes fabricated during this study are characterized by analyzing their spectral characteristics. A spectrophotometer (Shimadzu UV-2600) measures the reflectance and transmittance across a wavelength range of 300-1400 nm. In this case, the light spectrum determines the energy the membrane receives after filtration by the PV cell. The solar weighted spectral reflectance ( $\rho$ ) and transmittance ( $\tau$ ) of the membrane are calculated according to Equations (2.1) and (2.2). Moreover, the solar weighted spectral absorbance ( $\alpha$ ) is calculated according to Equation (2.3) [60]:

$$\rho = \frac{\int_0^{\infty} \rho_{\lambda} E_{\lambda} d\lambda}{\int_0^{\infty} E_{\lambda} d\lambda} \quad (2.1)$$

$$\tau = \frac{\int_0^{\infty} \tau_{\lambda} E_{\lambda} d\lambda}{\int_0^{\infty} E_{\lambda} d\lambda} \quad (2.2)$$

$$\alpha = 1 - \tau - \rho \quad (2.3)$$

Where  $\rho_{\lambda}$  is the spectral reflectance,  $\tau_{\lambda}$  is the spectral transmittance, and  $E_{\lambda}$  is the spectral emissive power obtained from ASTM – G173.

A preliminary analysis of the trial membranes doped with different nanoparticles, specified in Table 2.1, was conducted to identify the best possible option for doping purposes. The analysis also determined the amount of nanoparticles added during the synthesis process. The type of nanoparticles and the weight percent ratio presenting the highest absorbance from this analysis were selected to pursue the project's objectives. Subsequently, the final plain and doped membranes are characterized in the same manner.

#### **2.4. Morphological Characterization**

The membrane morphological structure is characterized by examining the top and bottom surfaces, the cross-sectional structure, the pore dispersion, and the dimensions. A Field Emission Scanning Electron Microscopy (FESEM, FEI Teneo) is used to obtain images of the membrane surfaces as well as of the cross-section at a micro-scale. The membrane is immersed in a liquid nitrogen bath for a few minutes, and then it is removed and shattered into small pieces for samples with clean-cut edges. A sample is glued to a stub by carbon tape and placed in a sputtering system. The sample is sputter coated with a thin layer of chromium prior to imaging for higher quality results. After the preparation of the sample, the stub is placed in the SEM chamber.

The membrane hydrophobicity is characterized by examining the contact angle (CA). A goniometer (Ramé-hart Model 90) equipped with imaging software (DROPimage CA) measures the angle between the membrane surface and a drop of DI water by the sessile drop method. First, the goniometer is calibrated according to the manufacturer specifications. Next, the membrane is positioned flat over the specimen stage, and the microsyringe carefully deposits a DI water drop on top of the membrane.

The software measures the contact angles between the membrane surface and both sides of the drop. The mean value of both angles, automatically calculated by the software, is the actual CA value. A total of twelve measurements from two different locations are averaged for consistency and reported as the CA in the following sections.

Three membranes are considered for this morphological characterization. Both final plain (Plain\_0.0\_Y\_250) and doped (C-Cu\_0.8\_Y\_250) membranes fabricated following the custom developed synthesis process are compared to a purchased commercial membrane. The commercial membrane selected for comparison is a PVDF membrane (Millipore GVHP00010), which does not contain nanoparticles.

## **2.5. Optical Results**

According to the preliminary analysis of the nanoparticles' optical properties, the copper nanopowder coated with black carbon presents the best absorptance. Figure 2.4 proves this statement by showing the results of all three nanoparticles considered. Based on this result, the carbon coated copper nanopowder is adopted for doping purposes. Additionally, the notch in the absorptance performance observed at the transition from the visible to the infrared spectrum is attributed to noise in the system.

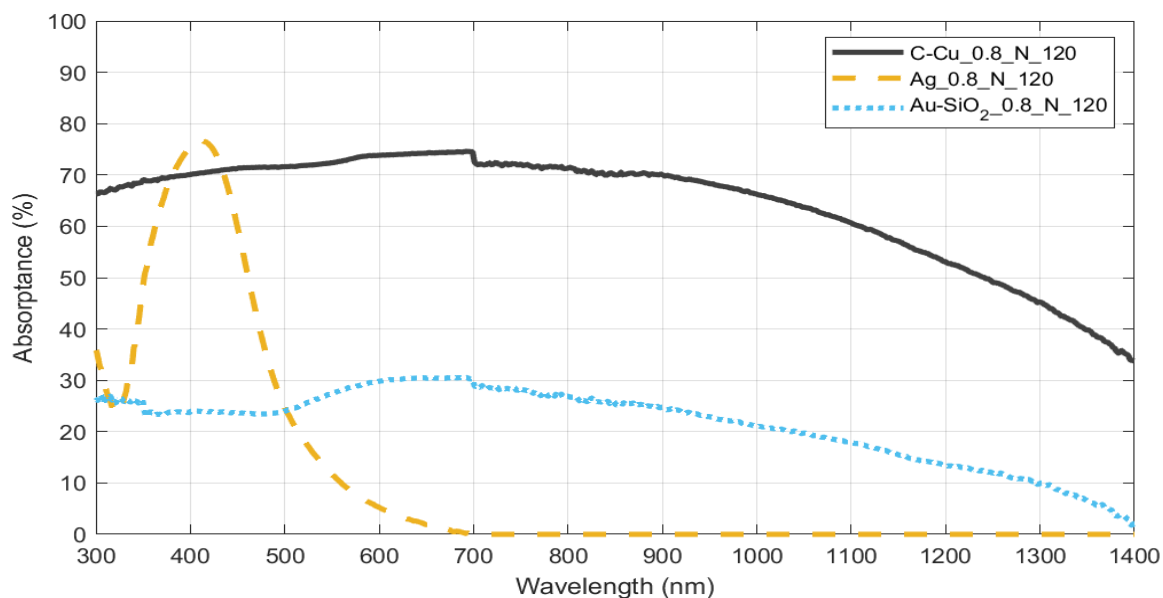


**Figure 2.4. Spectral Absorbance of the Trial Doped Membranes Fabricated via Phase Inversion**

Moreover, Table 2.2 proves that the addition of 0.8wt% NP at a thickness greater or equal to  $240\mu\text{m}$  provides a solar weighted spectral absorbance above 90%. This substantial increase of absorbance, in addition to the small variation of the membrane chemical composition, leads to the selection of 0.8wt% NP as the doping concentration of the final doped membrane. The preliminary analysis results lead to the selection of the membranes “Plain<sub>0.0</sub>Y<sub>250</sub>” and “C-Cu<sub>0.8</sub>Y<sub>250</sub>” for the completion of this project’s objectives. Furthermore, the membranes “Plain<sub>0.0</sub>Y<sub>250</sub>” and “C-Cu<sub>0.8</sub>Y<sub>250</sub>” will be referred to as “Plain Membrane” and “Doped Membrane”, respectively, throughout the remainder of this document.

**Table 2.2. Summary of the Membrane Composition and Weighted Spectral Absorptance at Different Carbon Coated Copper Nanopowder Weight Percent Ratios**

Membrane Name	NWS Type	Casting Thickness ( $\mu\text{m}$ )	PVDF (wt%)	DMF (wt%)	NP Type	NP (wt%)	Absorptance (%)
<i>C-Cu_0.1_N_120</i>	None	120	15.6	83.6	C-Cu	0.1	40.3
<i>C-Cu_0.1_N_240</i>	None	240	15.6	83.6	C-Cu	0.1	63.2
<i>C-Cu_0.8_N_120</i>	None	120	15.6	83.6	C-Cu	0.8	69.0
<i>C-Cu_0.8_N_240</i>	None	240	15.6	83.6	C-Cu	0.8	92.3
<i>C-Cu_0.8_Y_250</i>	Novatexx 2483	250	10.2	89.0	C-Cu	0.8	83.1
<i>C-Cu_2.4_Y_250</i>	Novatexx 2483	250	9.4	88.2	C-Cu	2.4	91.4

The plain membrane (Plain\_0.0\_Y\_250) used during this study exhibits a high reflectance and a near zero absorptance across the selected wavelength range, which results in a lower permeate flux due to the temperature polarization effect and a higher thermal input required for the feed stream when exposed to solar irradiance. Specifically, the weighted spectral reflectance and absorptance are 96.4% and 3.5%, respectively. Figure 2.5 exhibits the optical characterization of the plain membrane.

Contrasting with these results, the doped membrane (C-Cu\_0.8\_Y\_250) exhibits a substantial increase in absorptance and thus, a reduction in reflectance. Specifically, the weighted spectral reflectance and absorptance are 14.6% and 83.1%, respectively. Figure 2.6 exhibits the optical characterization of the doped membrane. Moreover, the stable results prove the uniform dispersion of copper (Cu) carbon coated NPs across the membrane structure and approve the synthesis process previously developed.

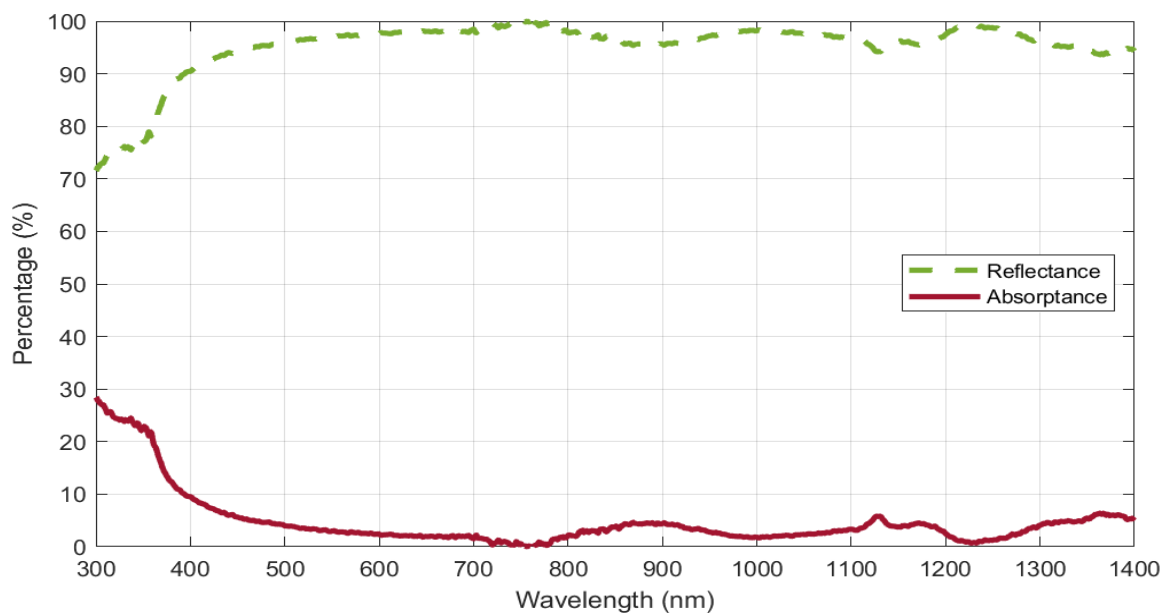


**Figure 2.5. Spectral Optical Properties of the Plain Membrane Fabricated via Phase Inversion**

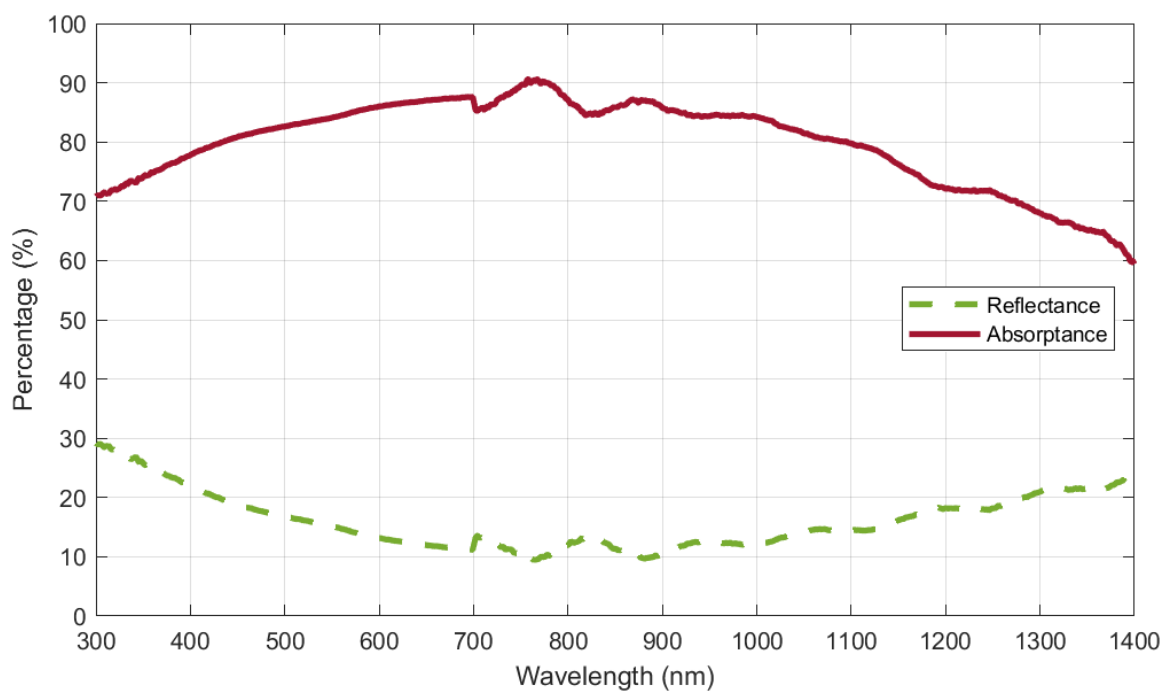


**Figure 2.6. Spectral Optical Properties of the Doped Membrane (0.8 wt% Copper Nanopowder Carbon Coated) Fabricated via Phase Inversion**

In a direct comparison between both membranes, Figure 2.7 exhibits the significant effect in the spectral absorptance performance of the small addition of NP. For

this case, the doped membrane improved its weighted spectral absorptance across the wavelength range by 79.6%.

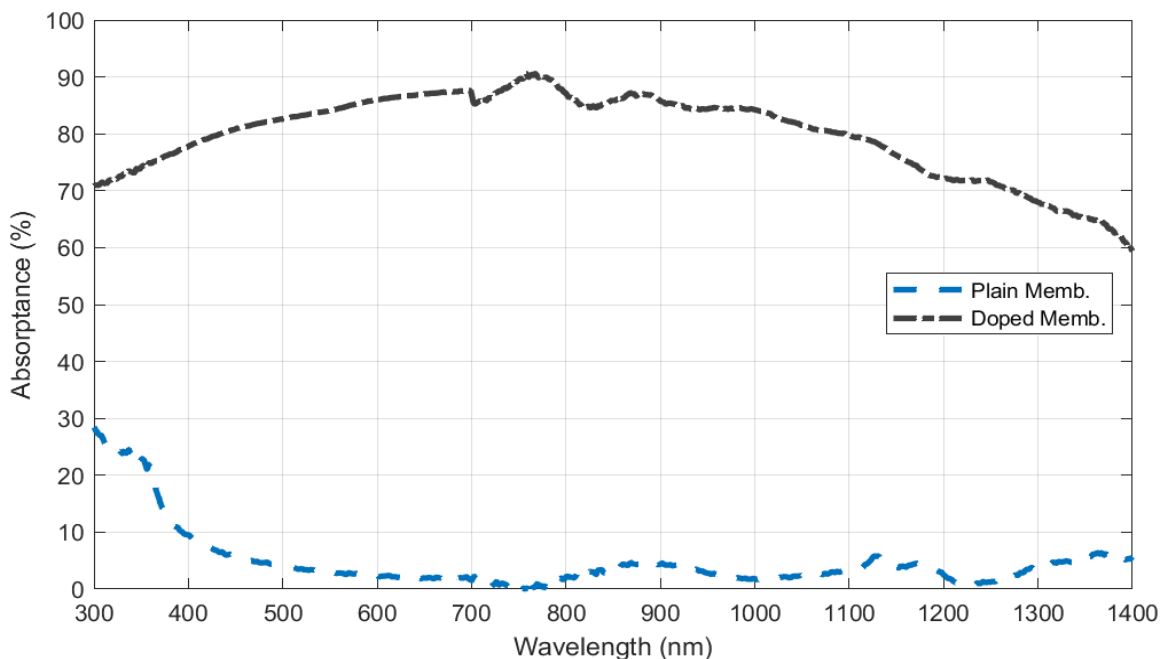


**Figure 2.7. Spectral Absorptance Comparison Between the Plain and Doped Membranes**

**Table 2.3. Summary of Weighted Spectral Absorptance of the Membranes Doped with Different Nanoparticles**

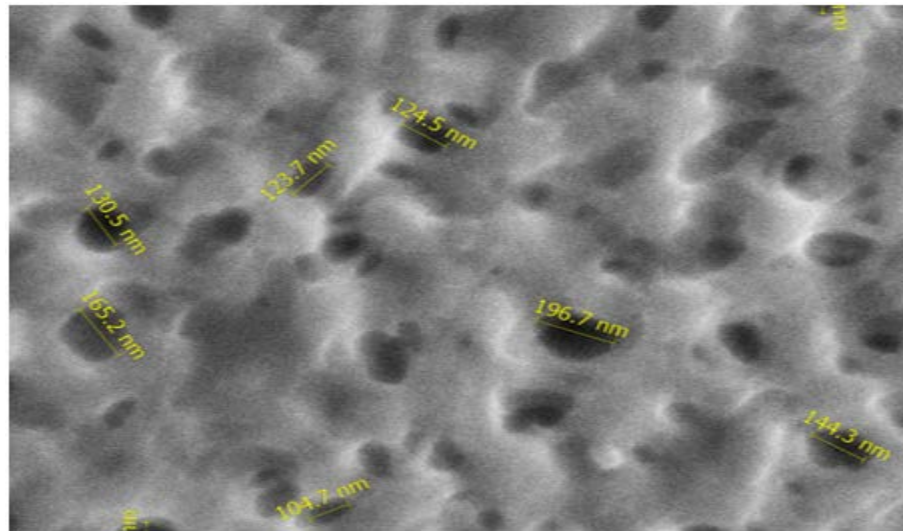
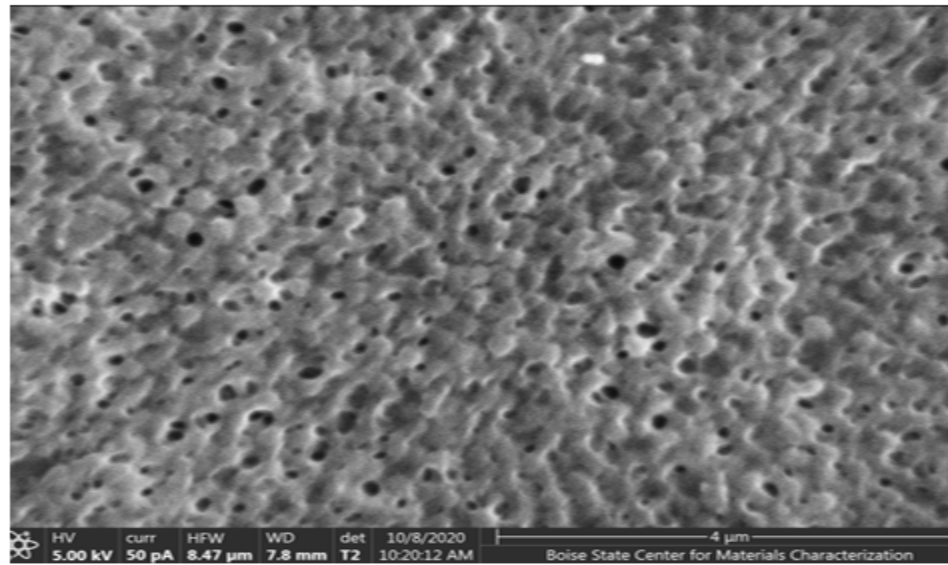
Membrane Name	“Plain” Plain_0.0_ Y_250	“Doped” C-Cu_0.8_ Y_250	C-Cu_0.8_ N_120	Ag_0.8_ N_120	Au-SiO <sub>2</sub> _0.8_ N_120
<i>Absorptance (%)</i>	3.5	83.1	69.0	10.9	24.6

## 2.6. Morphological Results

The morphology and cross section of the plain and doped membranes are displayed in the following images. The top and bottom surfaces exhibit the pore dispersion and dimensions, while the cross-section exhibits the structure, thickness, and bonding to the non-woven support. Figure 2.8 displays the top and cross section of the

plain membrane; Figure 2.9 displays the top and cross section of the doped membrane; Figure 2.10 displays the top surface and cross section of the commercial membrane.

a) Top Surface



b) Cross-section

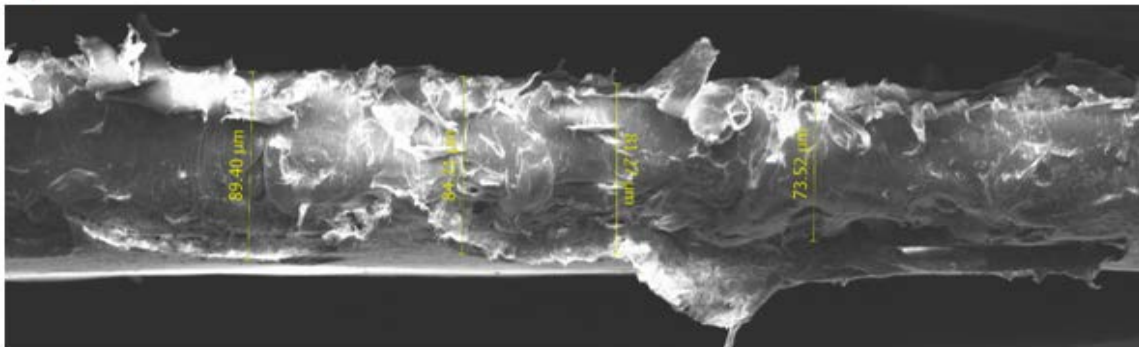
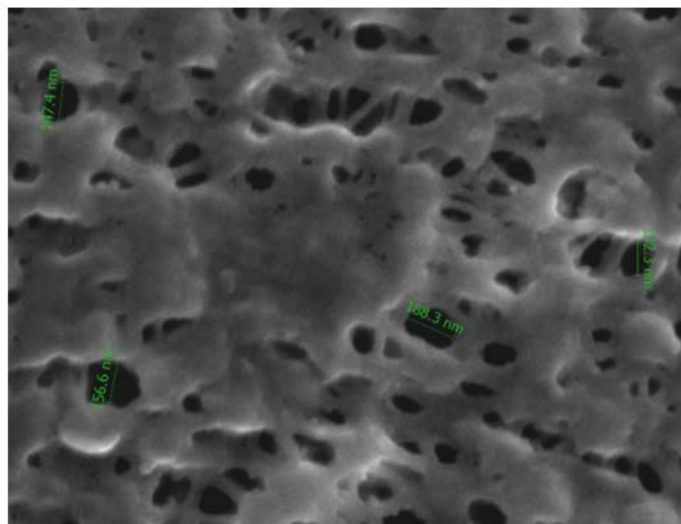
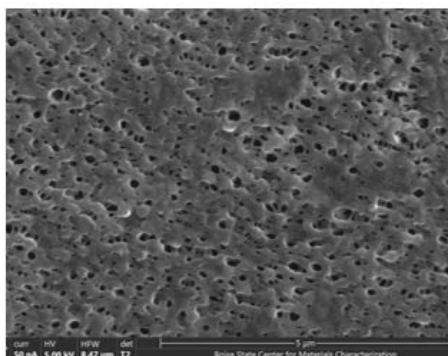
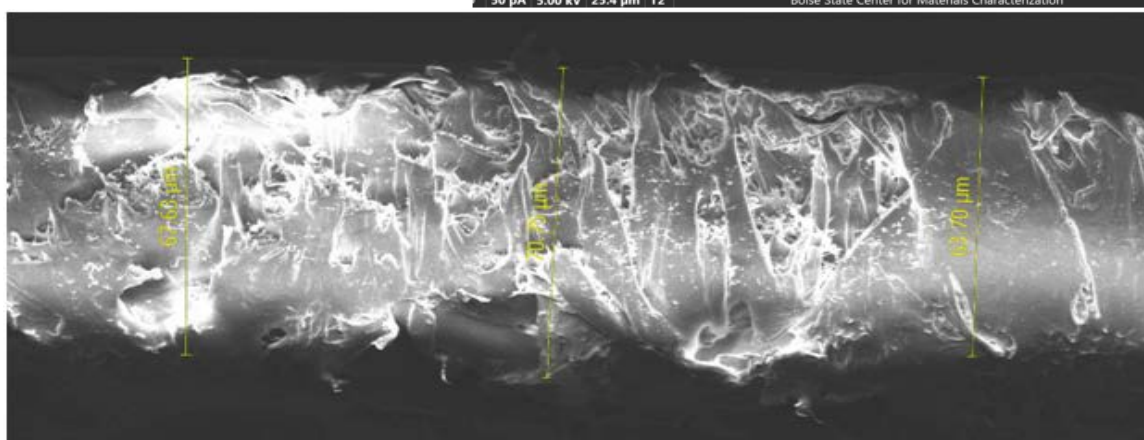
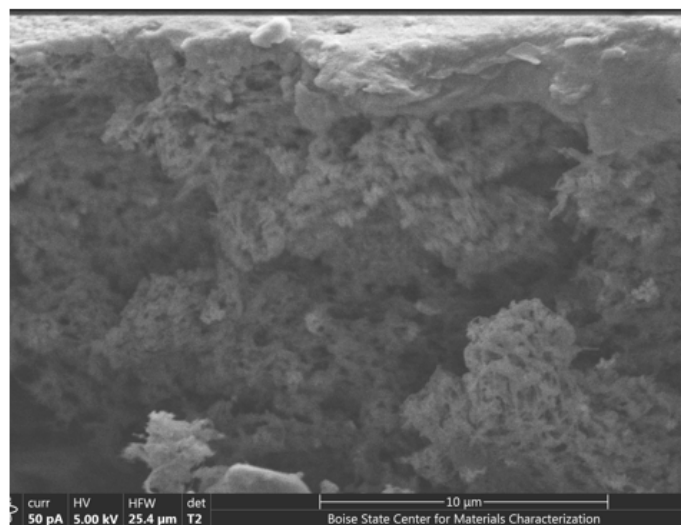


Figure 2.8. SEM Images of the Plain Membrane Fabricated via Phase Inversion:  
a) Top Surface, b) Cross Section

a) Top Surface

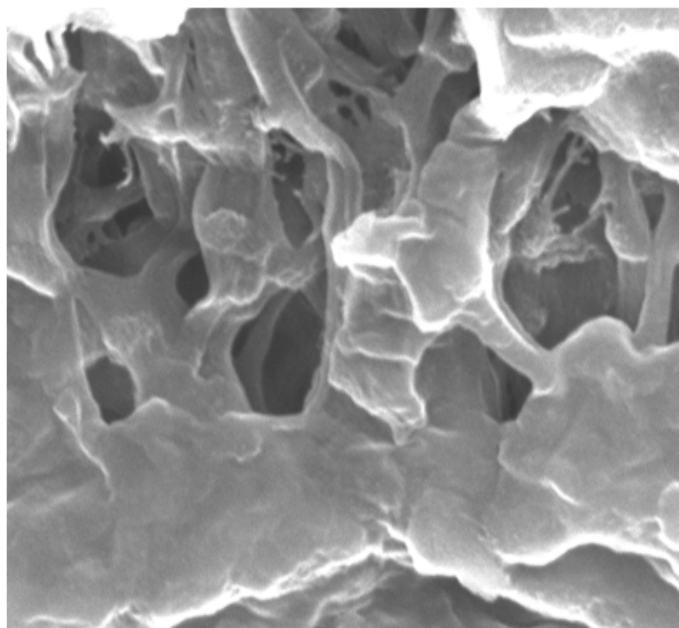
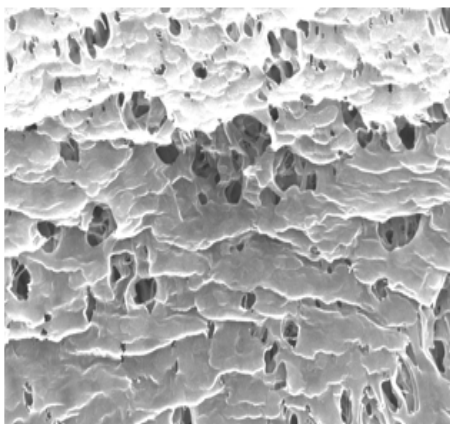


b) Cross-section



**Figure 2.9. SEM Images of the Doped Membrane Fabricated via Phase Inversion:**  
a) Top Surface, b) Cross Section

a) Top Surface



b) Cross-section

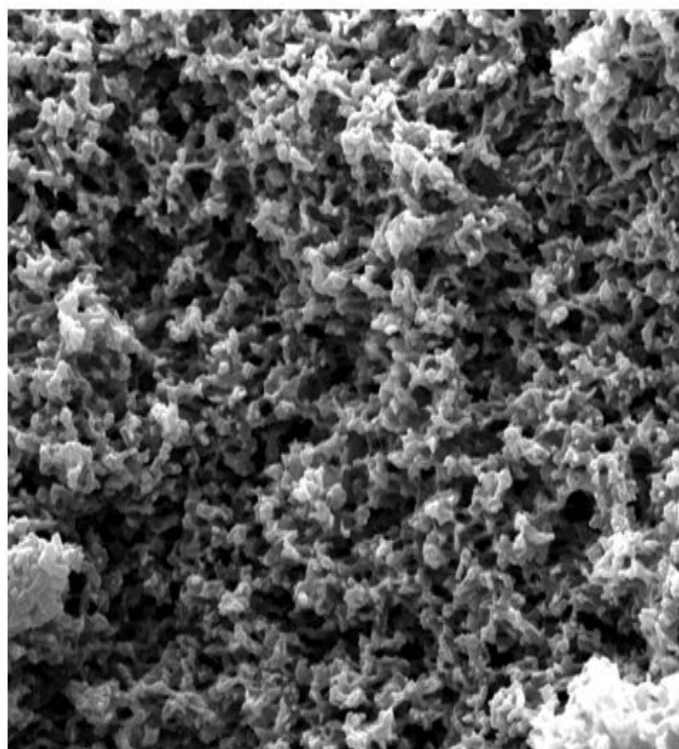
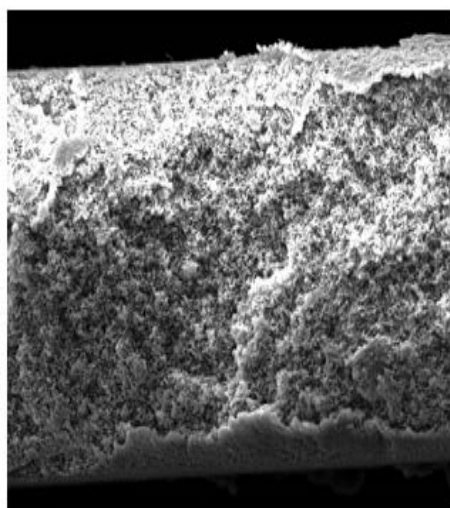


**Figure 2.10. SEM Images of a Commercial PVDF Membrane: a) Top Surface, b) Cross Section**

The plain and doped membranes exhibit a microporous structure with a consistent pore distribution along the surface and a pore size diameter range of 100-200nm, which qualify under the MD category specified in Table 1.1. The microporous structure also

proves the high miscibility between the polymer and the solvent [21]. Moreover, the pores exhibit an elliptical shape rather than circular, which results in a lower tortuosity and therefore, a lower permeate flux. Although a clean-cut edge of the membranes was not always obtained due to fracture resistance, the cross sections exhibit an approximate membrane final thickness between 60 and 80 $\mu\text{m}$ . In the case of the doped membrane, the structure and bonding to the support are observed. A sponge-like structure is displayed on top of the NWS fibers, confirming the hydrophobic nature of the membrane surface [21]. Similarly, the structure of a commercial membrane in Figure 2.10 exhibits sponge-like structures lacking macrovoids for a hydrophobic surface. The absence of visible particles in the doped membrane images demonstrates proper mixing and uniform dispersion. Therefore, ultrasonication is a successful technique to incorporate nanoparticles into the membrane solution.

The contact angle measurements obtained for all three membranes are summarized in Figure 2.11. The results exhibit a value of just over 100 degrees for both custom-made membranes, proving their hydrophobicity and capability for membrane distillation applications. The small load of NPs added to the doped membrane does not manifest an evident effect on its hydrophobicity as both values are similar. Moreover, their equivalent CA would theoretically translate to a similar desalination performance under no influence of any type of irradiance. However, this statement will be verified during the experimental section of the next chapter. In addition, these results are analogous to the commercial membrane, used in industrial applications, which provides more evidence of the successful synthesis process developed.

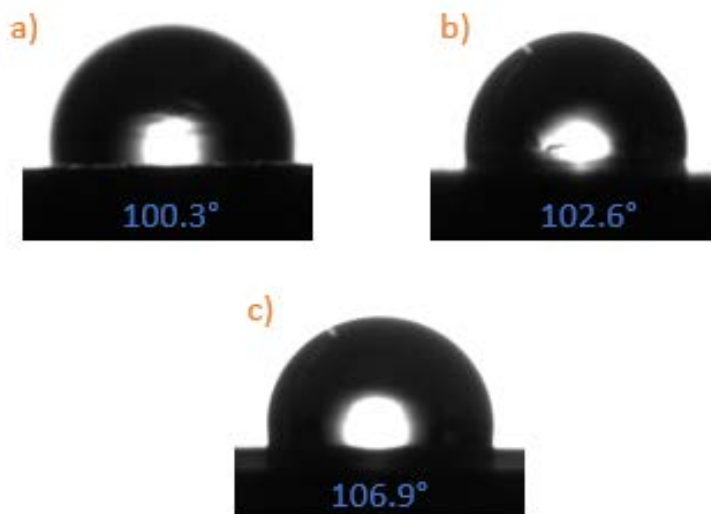


**Figure 2.11. Membrane Contact Angle Images and Measurements: a) Plain Membrane, b) Doped Membrane, c) Commercial Membrane**

## 2.7. Conclusions

This chapter investigated the first high level objective of the study. First, the development of a phase inversion process for the fabrication of membranes excluding or including nanoparticles has been proven by analyzing the membranes' optical and morphological properties. SEM images demonstrate the porosity, thickness, and microporous structure of the membranes fabricated. The uniform dispersion of nanoparticles across the membrane structure is demonstrated by their absence in the SEM images as well as the stable optical results, including absorbance and reflectance. The membrane hydrophobicity is confirmed by contact angle measurements above  $100^\circ$  and the analogous comparison to a commercial membrane. Second, the energy absorption enhancement of the membranes is proven by the optical analysis, specifically by the solar absorbance. The membrane doped with carbon coated copper nanopowder demonstrated an increment of 76.9% weighted spectral absorbance over the plain membrane without nanoparticles.

In order to accomplish the desalination characterization of the fabricated membranes, a test apparatus is required. The experimental apparatus's development is directly related to the second high level objective of this study and therefore, it is presented in the next chapter.

## CHAPTER THREE: HYBRID MEMBRANE DISTILLATION AND PHOTOVOLTAIC CELL SYSTEM DESIGN AND CHARACTERIZATION

This chapter focuses on the second high level objective of the study. Specifically, the design, construction, and performance characterization of a hybrid membrane distillation and photovoltaic cell system incorporating the proposed membrane module.

### **3.1. DCMD Setup**

The hybrid system design consists of a custom lab-scale DCMD configuration with the proposed PV-membrane module at the core of the system. The system includes two closed loops, the feed and the permeate, that will provide the required experimental conditions and a data acquisition system to log the data. Figures 3.1 and 3.2 exhibit a scheme of the system design and a picture of the system, respectively. The feed loop, or hot loop, consists of thermocouples (Omega TC-T-NPT-G-72) and pressure transmitters (Wika A-10) in the inlet and the outlet of the membrane module, a peristaltic pump (Masterflex L/S precision pump HV-77916-10), a heater (Intelligent heater QDWS1.0), and a water tank. The water running through this closed loop is a mixture of deionized (DI) water and salt (NaCl, BioXtra,  $\geq 99.5\%$  from Sigma Aldrich). The permeate loop, or cold loop, consists of the same thermocouples, pressure transmitters, water tank, and peristaltic pump. However, a cooling bath (Artic A10 refrigerated circulator 1525108) replaces the heater, and a conductivity meter (HM Digital PSC-64D) and an electronic balance (UWE OAC-12) are included. The water running through this loop is DI water,

through which the salt concentration is determined by measuring its electrical conductivity.

The data acquisition system consists of a chassis (NI cDAQ-9174) populated with a current module (NI-9203) and a temperature module (NI-9213), connected to a laptop to log the data using LabView software. The temperature module logs the temperature at the inlet and at the outlet of both loops. In contrast, the current module logs the pressure at the inlet and at the outlet of both loops and the electrical conductivity of the water in the permeate loop.

The same plain commercial PVDF membrane, used previously for a morphological comparison, is used to verify the functionality of the design. Moreover, both membranes, plain and doped, which were fabricated through the custom developed phase inversion process, are used in this study for performance characterization at indoor and outdoor conditions.

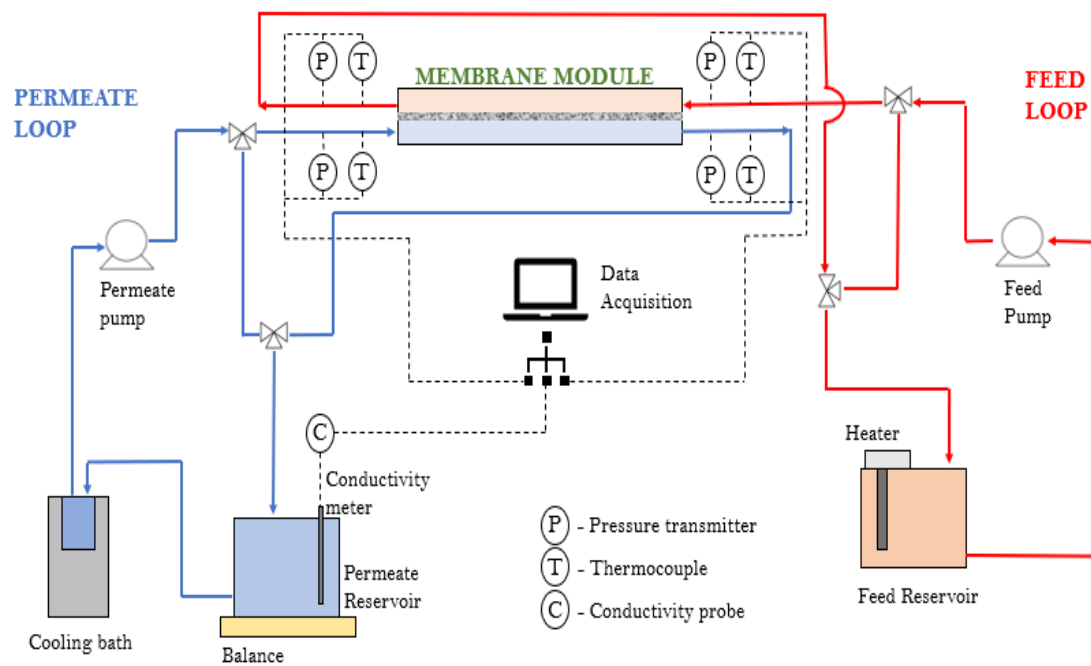


**Figure 3.1. Schematic Diagram of the Proposed Experimental System Design for the Membrane Performance Characterization**

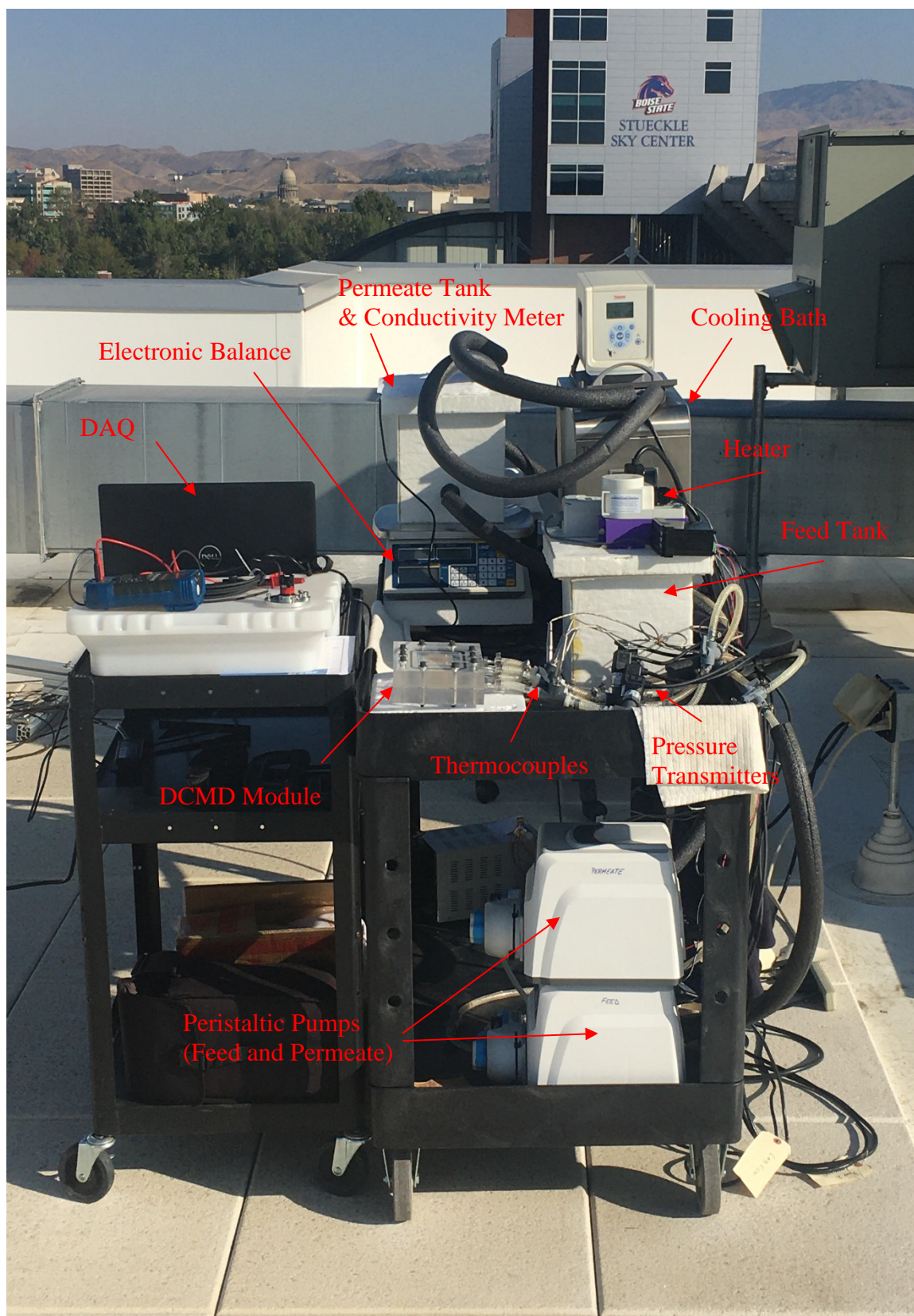


**Figure 3.2. Hybrid Membrane Distillation and Photovoltaic Cell System Setup for Outdoor Performance Characterization**

### 3.2. Hybrid System Characterization

#### Solar Module Characterization

Three semi-transparent solar modules (CdTe thin film from SolarFirst) rated at 30, 40, and 60% transparency and one solar module (amorphous silicon kindly provided by Onyx Solar), rated at 30% transparency, are considered in this study and displayed in Figure 3.3. The nomenclature to identify the solar modules is the following: “Module type\_Transparency(%)\_Module size (cm<sup>2</sup>)”.



**Figure 3.3. Semi-transparent Solar Modules: a) CdTe\_30%\_721, b) CdTe\_40%\_900, c) CdTe\_60%\_225, d) Silicon\_30%\_144**

**Table 3.1. Summary of Solar Modules Characteristics**

Solar Module Name	Module Type	Transparency (%)	Size (cm <sup>2</sup> )
<i>CdTe_30%_721</i>	CdTe	30	721
<i>CdTe_40%_900</i>	CdTe	40	900
<i>CdTe_60%_225</i>	CdTe	60	225
<i>Silicon_30%_144</i>	Silicon	30	144

The solar modules are optically characterized using a miniature spectrometer (FLAME-S-XR1-ES) and a spectrophotometer (Shimadzu UV-2600) by determining their transmittance ( $\tau$ ). In the case of the miniature spectrometer, a spectral intensity is provided across a wavelength range of 200-1,000 nm. The transmittance is calculated by measuring the spectral intensity of the solar module and dividing it by a spectral intensity baseline test, without the solar module, as shown in Equation 3.1.

$$\tau_{\lambda} = I_{cell}/I_{baseline} \quad (3.1)$$

Where  $\tau_{\lambda}$  is the spectral transmittance (%) of the solar module,  $I_{cell}$  is the spectral intensity of the solar module (counts), and  $I_{baseline}$  is the spectral intensity baseline (counts).

On the other hand, the spectrophotometer provides the spectral transmittance across a wavelength range of 300-1,400 nm. The wavelength range is selected to determine the amount of light in the visible spectrum, 400-700 nm, that the solar modules transmit to the feed stream and ultimately to the membrane. Moreover, the solar modules under analysis seem to be embedded in architectural window glass, which provides filtration of the ultraviolet (UV) and the infrared (IR) spectrums. The potential irradiance filtration from the architectural glass is determined by measuring the transmittance of the

solar modules in the UV and IR spectrums. The thermal gain characterization is important since it can improve the performance by mitigating the membrane photothermal effect.

The performance and efficiency of the solar modules are measured by a solar power analyzer (Amprobe Solar 600) and a pyranometer (LI-COR LI-200R-BL-5). With a wavelength range of 400-1,100 nm, the pyranometer is used to measure the global horizontal solar irradiance before and during the experimental tests. It is connected to a multimeter to obtain a current output, which is then converted to an actual solar irradiance value. The measured irradiance and the solar module area are imported to the solar power analyzer. To characterize the solar module, kelvin clips probes are connected from the instrument to the solar module's poles, and an auto-scan is performed. The solar power analyzer is used to determine the module performance by recording the current and voltage (I-V) curve, the maximum solar power, and the solar module efficiency, among other values.

#### Desalination Characterization

An extensive number of experimental tests at different conditions are required to evaluate the performance of the hybrid design, including the plain and doped membranes and the PV cell on top of the membrane module. Tests at indoor conditions, with no solar irradiance, are used to determine the performance of both membranes, and tests at outdoor conditions are used to demonstrate the photothermal heating effect. This approach measures the repercussion of each design component.

A specific set of experimental conditions, defined as the standard testing conditions, are used to directly compare the membrane performance. These conditions

consist of the feed loop set at a temperature of 60°C, a flow rate of 900 mL/min, and a concentration of 10 ppt (parts per thousand); and the permeate loop set at a temperature of 10°C, a flow rate of 450 mL/min, and a concentration of 0 ppt. Moreover, the membrane performance is determined by varying one parameter while maintaining the remaining parameters at their standard values.

The characterization process is applied to both plain and doped membranes and includes a range of common MD operating conditions. The feed loop covers temperatures of 50-80°C at 10°C intervals, flow rates of 450-900 mL/min (200-400 rpm) at intervals of 225mL/min, and concentrations of 0-50 ppt at 10 ppt intervals to cover fresh, moderate, and highly saline waters above the common 35 ppt salinity of oceans [8]. The permeate loop is set at a temperature of 10°C, a flow rate of 450 ml/min, and a concentration of 0 ppt. Furthermore, each experimental test is recorded for 90 min and performed twice for data reliability.

The outdoor performance characterization is performed at the standard conditions for direct comparison to the indoor performance. In the case of the doped membrane, an additional test is conducted to characterize the effect of the PV cell in the membrane performance. As with the characterization process at indoor conditions, each experimental test is recorded for 90 min and performed twice for data reliability.

The membrane performance is evaluated by measuring the permeate flux (J) and the salt rejection (SR), which can be determined by the following equations [24]:

$$J = \frac{\Delta m}{A * \Delta t} \quad (3.2)$$

$$SR = \frac{C_f - C_p}{C_f} * 100 \quad (3.3)$$

The first equation is based on the weight change of the permeate tank over time.  $\Delta m$  is the mass increase of permeate water,  $A$  is the effective membrane area (42 cm<sup>2</sup> for this study), and  $\Delta t$  is the sampling time. The second equation is based on the initial and final conductivity of the feed and the permeate solutions.  $C_f$  and  $C_p$  are the feed and permeate concentration, respectively.

### **3.3. Hybrid System Results**

#### Solar Module Results

The 60% semi-transparent CdTe thin film solar module (CdTe\_60%\_225) and the 30% semi-transparent silicon solar module (Silicon\_30%\_144) are optically characterized in Figure 3.4. Both solar panels, commercially available, are embedded in architectural window glass. As a result, the two solar modules have very similar optical spectrums, despite having different bandgaps for the underlying solar module. Inherently, this glass limits the amount of infrared light transmission into the building envelope to limit infrared heating, contrary to the desired goal here. Qualitatively, this can be seen in the green tinting observed in the back-glass layer in which the PV cell is contained. Obtaining cells contained between two plates of low-iron float glass would be ideal but are not available without a custom order.

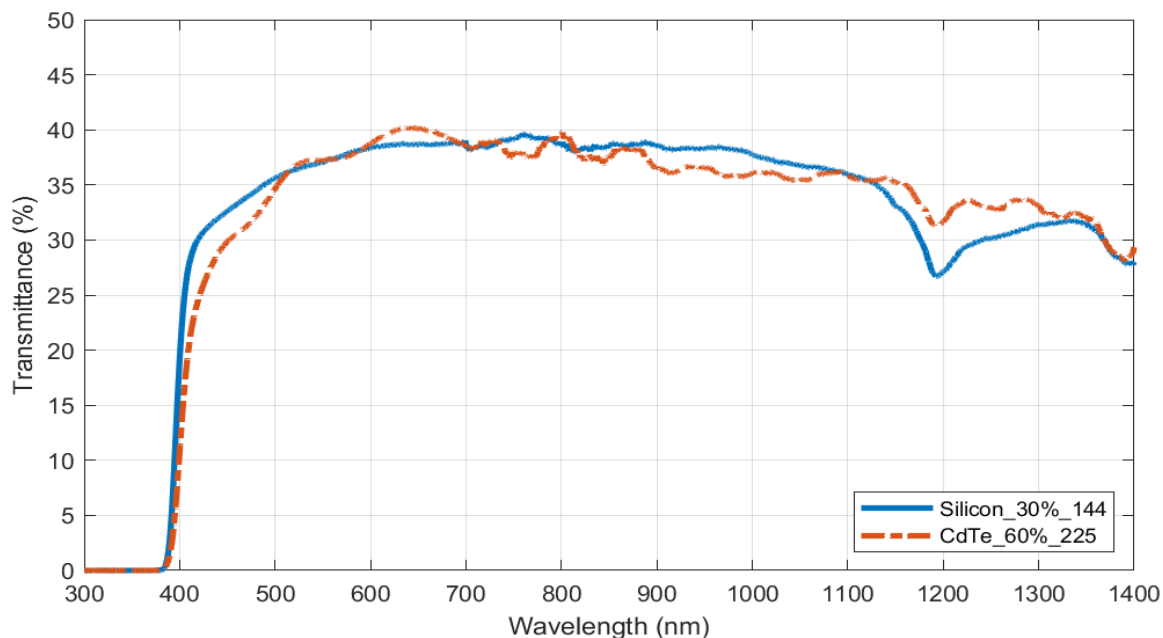


**Figure 3.4. Spectral Transmittance of Two Types of Solar Modules (CdTe\_60%\_225 and Silicon\_30%\_144) Used in Architectural Glass Applications**

The spectral intensity and transmittance characterization of the three CdTe thin film solar modules is shown in Figure 3.5. In the left graph, the intensity data and a baseline test is used for the transmittance calculations. The intensity data was recorded indoors and through a window to avoid reaching the apparatus upper limit and flattening the data in the visible spectrum, which would be expected if the data were taken outdoors. This fact explains the baseline test's low intensity values in the IR and UV spectrums and also the equivalent values for all the modules in those wavelength ranges. The CdTe\_60%\_225 module shows the best intensity in the visible spectrum due to the higher transparency, as expected, while the CdTe\_30%\_721 and the CdTe\_40%\_900 modules show comparable performances. Characterization of these two modules with a solar analyzer can provide more details to explain these results. The transmittance, right graph, is calculated according to Equation 3.1. The transmittance is close to unity for the IR and UV spectrums due to performing the test indoors. As in the intensity results, the

CdTe\_60%\_225 module shows the best transmittance in the visible spectrum, while the other two CdTe modules show comparable performances.

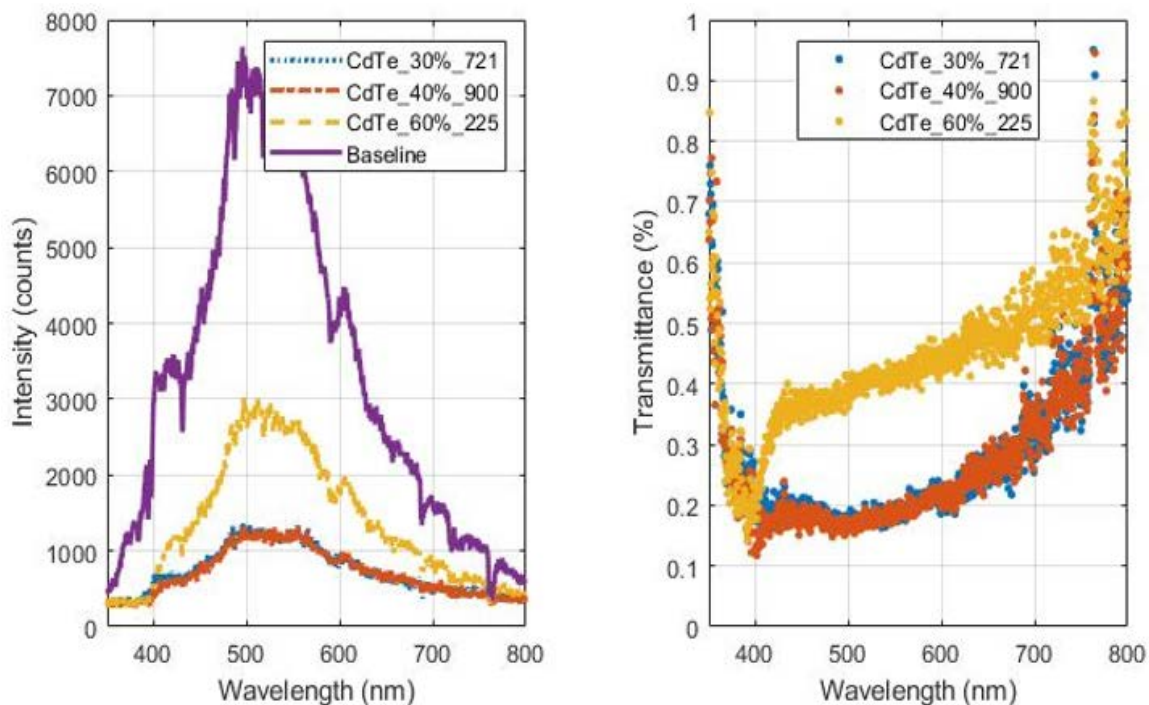


**Figure 3.5. Spectral Intensity and Transmittance of Three Semi-transparent CdTe Solar Modules (CdTe\_30%\_721, CdTe\_40%\_900, and CdTe\_60%\_225)**

The performance and efficiency characterization, including the current-voltage (I-V) and power (W) curves, of the CdTe thin film solar modules is shown in Figure 3.6. Table 3.2 also summarizes this characterization. The efficiency ( $\eta$ ) is used for comparison due to the different dimensions of the solar modules. The CdTe\_30%\_721 solar module exhibits an efficiency close to 5%, which is well below commonly seen commercial modules but typical of semi-transparent window modules such as the ones utilized here. Furthermore, the CdTe\_60%\_225 module exhibits the lowest efficiency among the solar modules, due to its higher transparency. The fill factor (FF), another performance indicator, is used to identify the presence of a defect or degradation of the solar module. In this case, a more triangular shape instead of the expected squared shape

is observed in the IV curve for the CdTe\_40%\_900 solar module (Figure 3.6B), which indicates an abnormality in the module and explains the previously obtained result in

Figure 3.5.

**Table 3.2. Summary of CdTe Thin Film Solar Panels Performance Characterization**

<b>Transmittance (%T)</b>	<b>Vopen (V)</b>	<b>Isc (mA)</b>	<b>Pmax (W)</b>	<b>Vmax (V)</b>	<b>Imax (mA)</b>	<b><math>\eta</math> (%)</b>	<b>FF</b>	<b><math>\tau</math> (%)</b>
<i>CdTe_30%_721</i>	20.58	177	2.31	15.58	149	4.63	0.64	42.3
<i>CdTe_40%_900</i>	25.08	259	2.16	13.49	161	3.40	0.33	41.5
<i>CdTe_60%_225</i>	10.50	89	0.44	7.14	62	2.94	0.48	56.5

\*Vopen (open-circuit voltage)

\*Isc (short-circuit current)

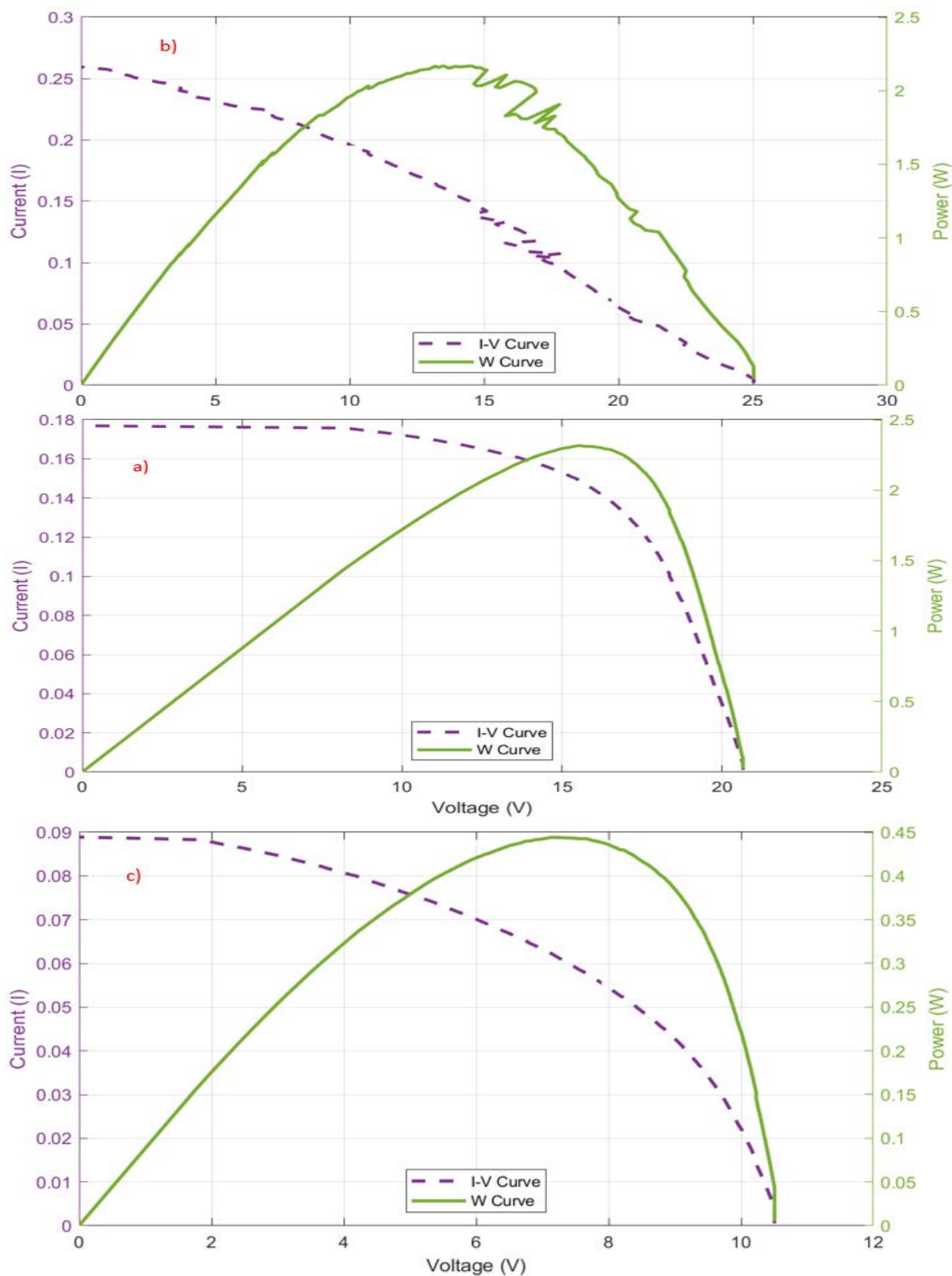
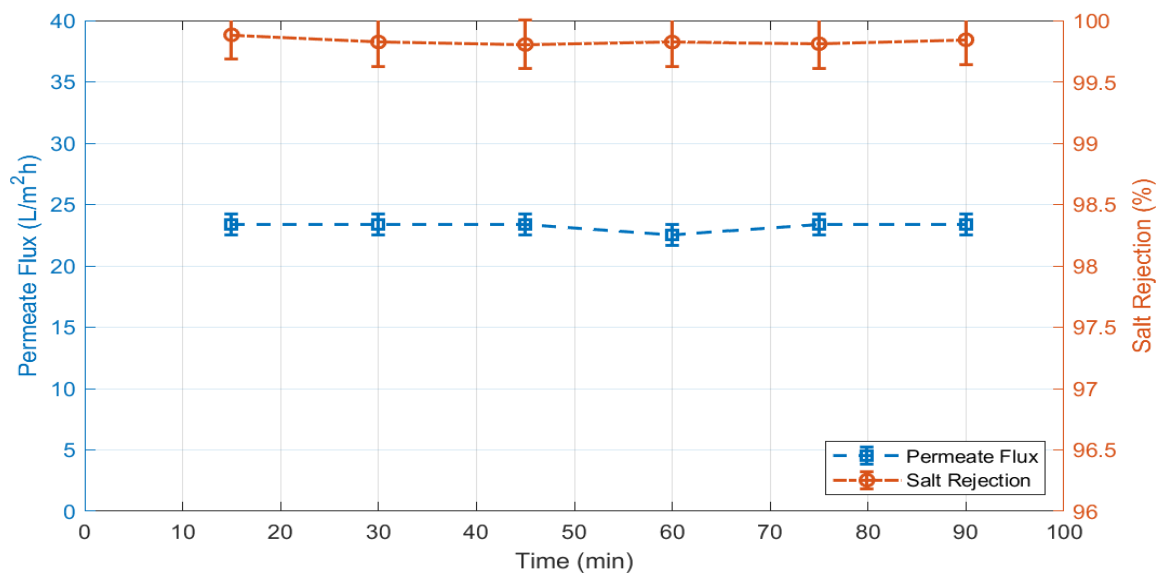


**Figure 3.6. Current-Voltage (I-V) and Power (W) Performance Curves of Three CdTe Thin Film Solar Panels: a) CdTe\_30%\_721; b) CdTe\_40%\_900; c) CdTe\_60%\_225**

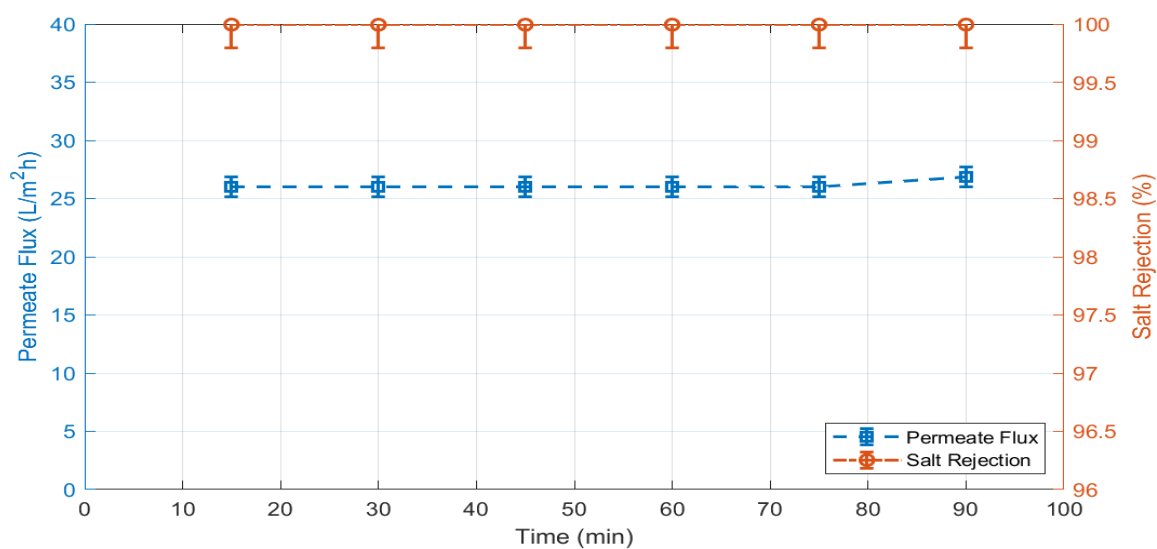
The 60% transparency CdTe solar module (CdTe\_60%\_225) was selected to be incorporated into the hybrid membrane distillation with PV cell due to its higher transmittance. The higher transmittance results in more solar irradiance transmission through the solar module to reach the membrane and, as a result, provide a higher mitigation effect of the temperature polarization. Although this solar module exhibits a low efficiency and fill factor, solar modules with better performance and contained between two low-iron float glass plates can be developed.

#### Desalination Results Off-Sun

Figures 3.7 and 3.8 exhibit the performance results of the plain (Plain\_0.0\_Y\_250) and the commercial (C-Cu\_0.8\_Y\_250) membranes at the standard conditions, respectively. Both membranes present a salt rejection above 99.8%, demonstrating their suitability for MD applications. Although they present a comparable performance, expected from the contact angle measurements, the doped membrane produces an overall higher permeate flux than the plain membrane, which can be attributed to the addition of nanoparticles [24,49]. The addition of nanoparticles affects the membrane properties, specifically the porosity and the hydrophobicity, leading to the difference in desalination performance. The membrane porosity could be a possible reason for the permeate flux increase, but it could not be verified here. A measurement is taken every 15 min for a total of six measurements for each test. However, only the last four measurements of each test are averaged and reported as the permeate flux result.



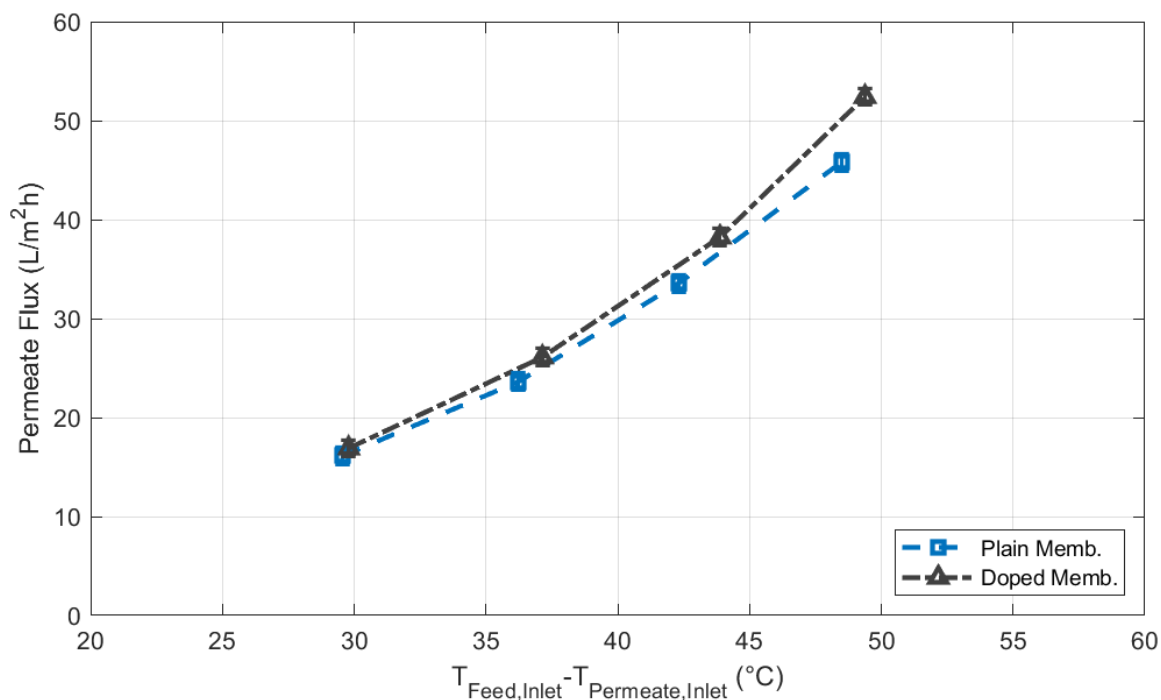
**Figure 3.7. Plain Membrane (Plain\_0.0\_Y\_250) Performance Off-Sun at Standard Conditions (Permeate Flux and Salt Rejection)**



**Figure 3.8. Doped Membrane (C-Cu\_0.8\_Y\_250) Performance Off-Sun at Standard Conditions (Permeate Flux and Salt Rejection)**

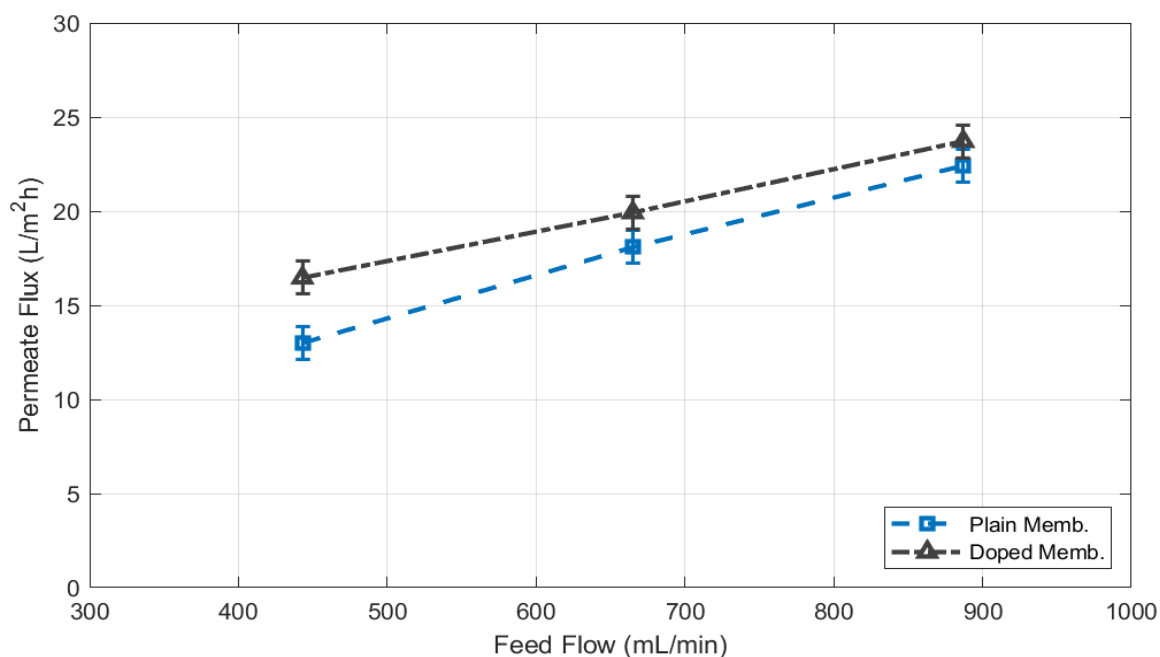
Figures 3.9, 3.10, and 3.11 exhibit the mapping characterization of the plain and the doped membranes during the different experimental conditions. Two tests at each experimental condition are performed, and the average of those two tests is reported here. The overall performance of both membranes is in accordance with the results of previous studies [18,34,49].

Figure 3.9 displays the performance of both membranes at different feed temperatures, while the remaining parameters are maintained at standard conditions. The temperature difference between the inlet feed and the inlet permeate streams is reported instead of the feed temperatures to provide a more accurate comparison. Both membranes exhibit an increase in the permeate flux as the feed temperature increases, which is expected for a thermally driven process. An increase in temperature results in an increase of the vapor pressure gradient between the feed and the permeate streams and thus, increases the driving force. Although the permeate flux at the lower temperatures is similar for both membranes, the doped membrane seems to perform slightly better than the plain membrane at the higher temperatures, which can be attributed to the addition of nanoparticles [49]. Both membranes maintained a salt rejection above 99.8% across all tests. In addition, the results obtained are in the range of previous studies [18,34,49].



**Figure 3.9. Plain (Plain\_0.0\_Y\_250) and Doped (C-Cu\_0.8\_Y\_250) Membranes Performance Off-Sun at Different Feed Temperatures (Remaining Experimental Conditions Maintained at Standard Conditions)**

Figure 3.10 displays the performance of both membranes at different feed flow rates, while the remaining parameters are maintained at standard conditions. As in the previous case, both membranes exhibit an increase in the permeate flux as the feed flow rate increases. An increase in the flow rate leads to an enhancement of the turbulence and mixing in the feed channel, resulting in a decrease in the thickness of the temperature boundary layer [18]. Both membranes maintained a salt rejection above 99.8% across all tests.



**Figure 3.10. Plain (Plain\_0.0\_Y\_250) and Doped (C-Cu\_0.8\_Y\_250) Membranes Performance Off-Sun at Different Feed Flow Rates (Remaining Experimental Conditions Maintained at Standard Conditions)**

Figure 3.11 displays the performance of both membranes at different feed concentrations, while the remaining parameters are maintained at standard conditions. In this case, both membranes exhibit a decrease in the permeate flux as the feed concentration increases. An increase in concentration leads to a reduction of the vapor pressure gradient, reducing the driving force. The contribution of the concentration

polarization to the temperature boundary layer results in a reduction of the driving force for evaporation [18,34]. Again, both membranes maintained a salt rejection above 99.8% across all tests.

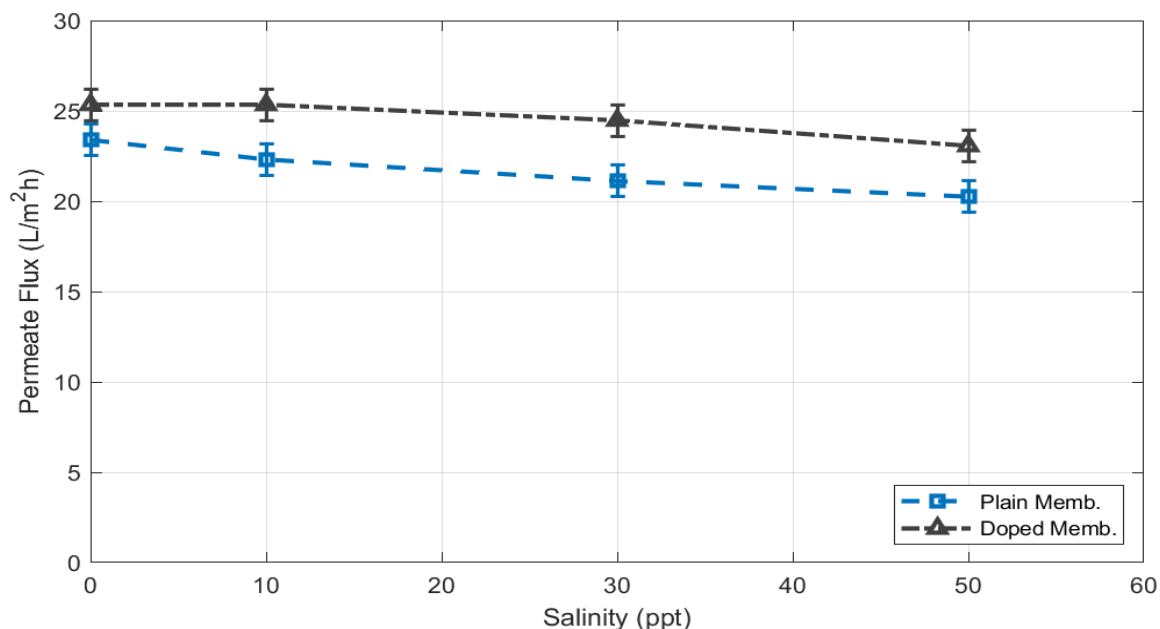
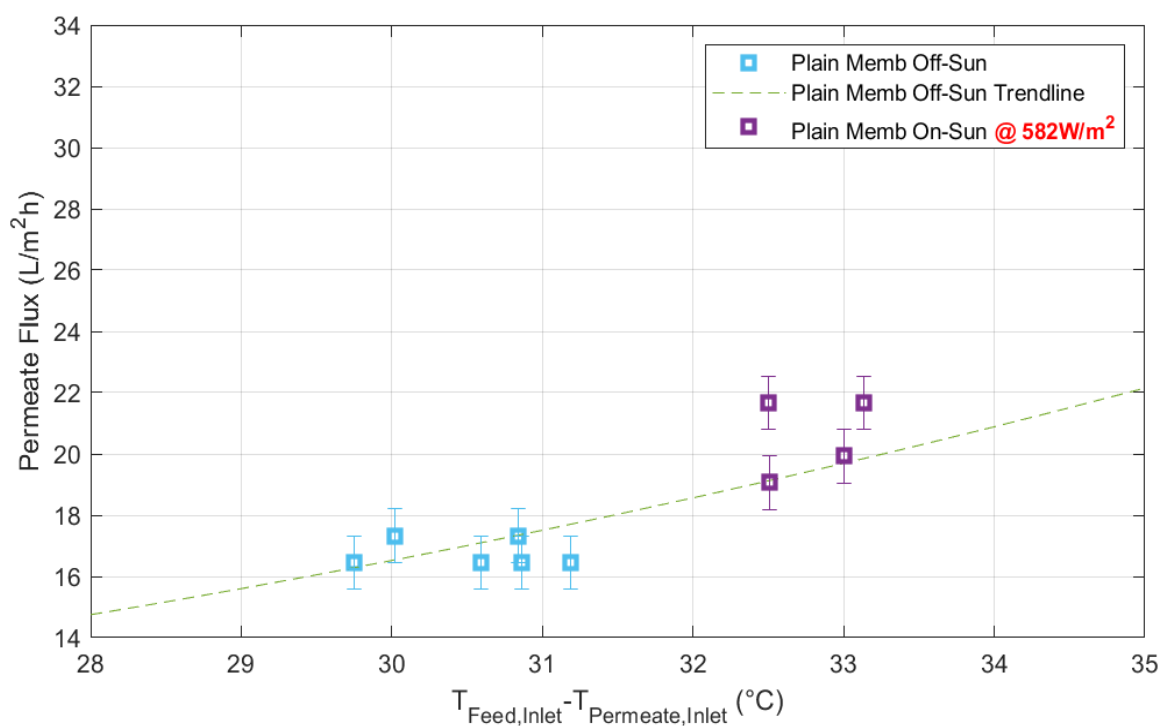


**Figure 3.11. Plain (Plain\_0.0\_Y\_250) and Doped (C-Cu\_0.8\_Y\_250) Membranes Performance Off-Sun at Different Feed Concentrations (Remaining Experimental Conditions Maintained at Standard Conditions)**

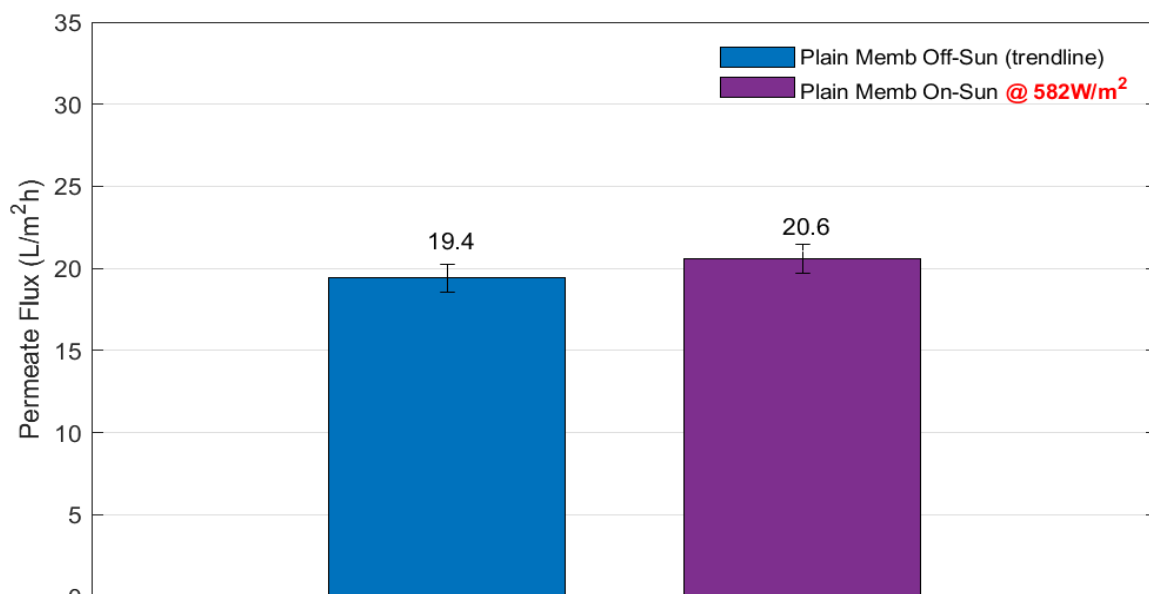
### Desalination Results On-Sun

Figure 3.12 exhibits the photothermal effect on the plain membrane (Plain\_0.0\_Y\_250) at standard conditions and Figure 3.13 summarizes the permeate performance at the same temperature difference. As with the permeate flux, the solar irradiance is averaged for the last four measurements of the test and reported as a single value. A trendline, calculated from the results at multiple temperatures in Figure 3.9, is included to provide another comparison indicator to the expected membrane performance at indoors conditions. In this case, an increase of 5.8% permeate flux was observed when exposed to a global horizontal irradiance (GHI) of 582 W/m<sup>2</sup>, which can be attributed to a

radiative heating effect [16,42]. Previous studies display a performance improvement for undoped membranes when exposed to laser radiation of concentrated intensity due to a radiative effect [42], which in this case, was observed at a smaller scale. This result was expected due to the high spectral reflectance obtained during the optical characterization of this membrane.



**Figure 3.12. Photothermal Effect on the Plain Membrane (Plain\_0.0\_Y\_250) at Standard Conditions. Comparison of Off-Sun to On-Sun Performances (GHI of 582W/m<sup>2</sup>)**



**Figure 3.13. Summary of the Photothermal Effect on the Plain Membrane (Plain\_0.0\_Y\_250) at Standard Conditions**

Figures 3.14 and 3.15 exhibit the photothermal effect on the doped membrane (C-Cu\_0.8\_Y\_250) during two tests at standard conditions. The doped membrane in both cases exhibits an increase in the permeate flux when exposed to solar irradiance. Specifically, the performance improved by 15.0% and 32.1% under a solar irradiance of 617 W/m<sup>2</sup> and 698 W/m<sup>2</sup>, respectively. This increase in permeate flux is attributed to the radiative effect and the addition of nanoparticles, which mitigates the temperature polarization phenomenon. The NPs act as nanoheaters inside the membrane, activated by the solar irradiance, to reduce the temperature polarization effect by increasing the membrane surface temperature [15]. The increase of the membrane surface temperature results in an increase in the vapor pressure gradient, ultimately enhancing the driving force of the process. In this case, an increase in performance was expected due to the significant increase of spectral absorption obtained during the optical characterization of this membrane.

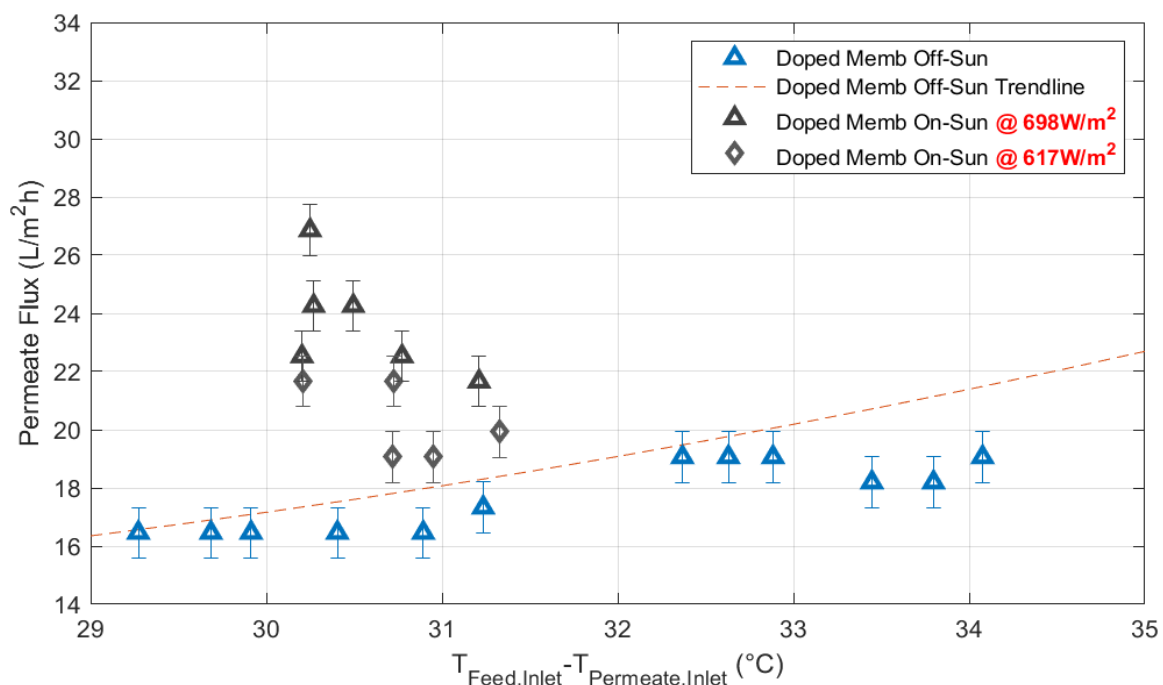


**Figure 3.14. Photothermal Effect on the Doped Membrane (C-Cu\_0.8\_Y\_250) at Standard Conditions. Comparison of Off-Sun to On-Sun Performances (GHI of 617 and 698  $\text{W}/\text{m}^2$ )**

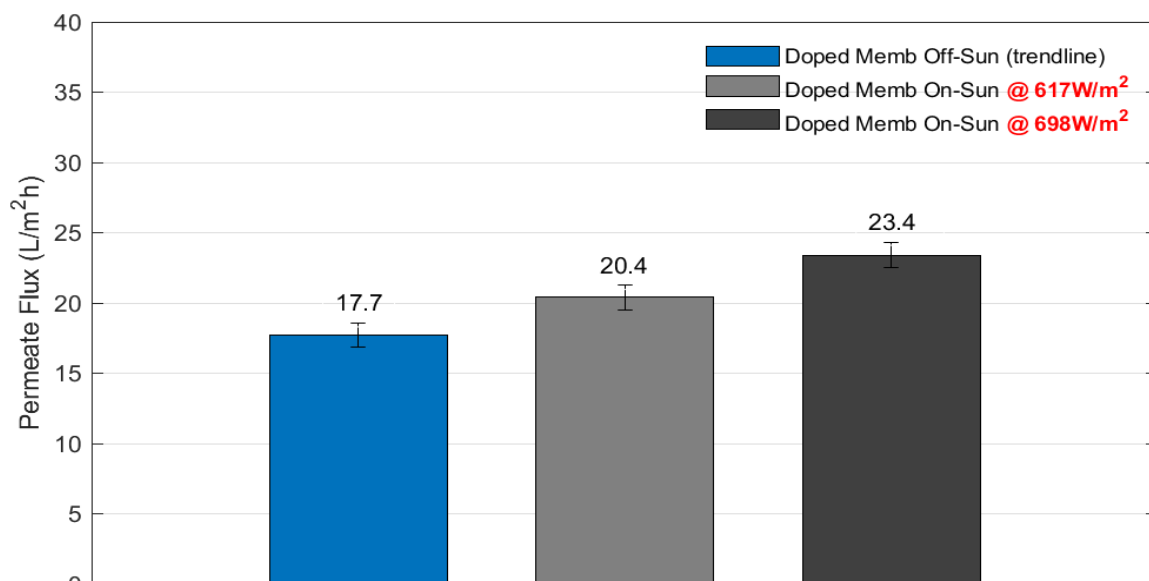


**Figure 3.15. Summary of the Photothermal Effect on the Doped Membrane (C-Cu\_0.8\_Y\_250) at Standard Conditions**

As a summary, Figure 3.16 combines the photothermal effect on the plain and doped membranes into one graph. The performance trendlines of both membranes at indoor conditions are also included.

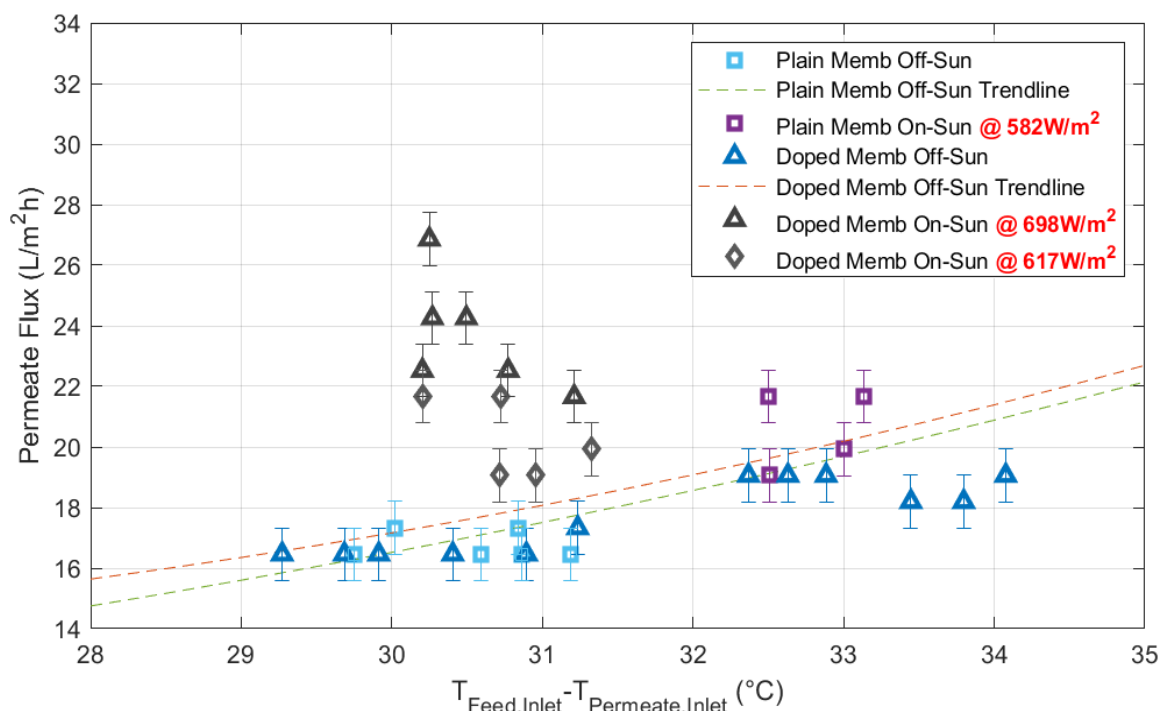


**Figure 3.16. Summary of the Photothermal Effect on the Plain Membrane (Plain\_0.0\_Y\_250) and the Doped Membrane (C-Cu\_0.8\_Y\_250) at Standard Conditions**

Figures 3.17 and 3.18 exhibit the effect of the solar module CdTe\_60%\_225 on the membrane performance at standard conditions, and Table 3.3 displays the experimental data recorded. In this case, the 60% transparency CdTe thin film solar module was placed on top of the membrane module and was exposed to a solar irradiance of 508 W/m<sup>2</sup>. The doped membrane exhibits an increase of the permeate flux comparable to the cases with the PV cell excluded. The addition of the PV cell on top of the DCMD module was expected to reduce the solar flux to the membrane, which would result in a permeate flux drop. However, the drop in permeate flux was not observed. Adding solar modules, embedded in 7 mm thick glass, on the front side (feed) of the DCMD module reduces the heat loss to the environment, likely increasing the performance.

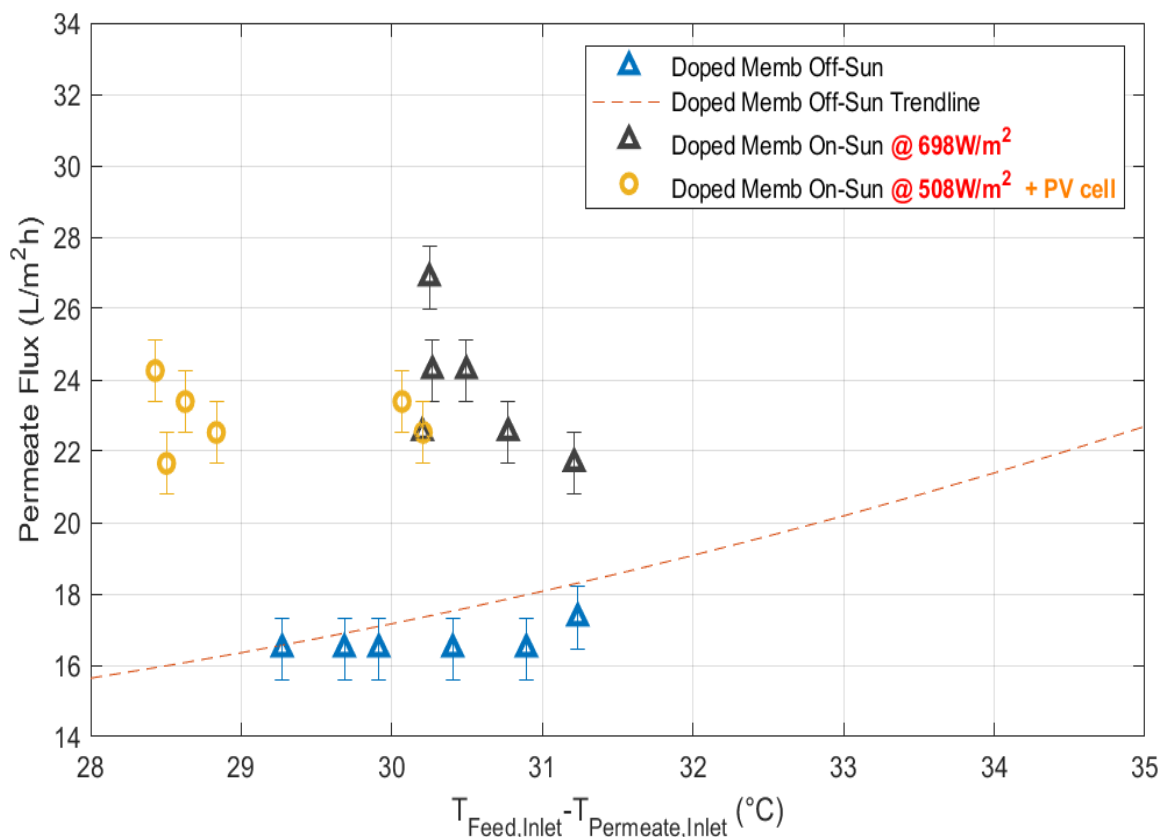


**Figure 3.17. Solar Module (CdTe\_60%\_225) Effect on the Photothermal Effect of the Doped Membrane (C-Cu\_0.8\_Y\_250) at Standard Conditions. Membrane Performance Including and Excluding the Solar Module (GHI of 508 and 698 W/m<sup>2</sup> Respectively)**

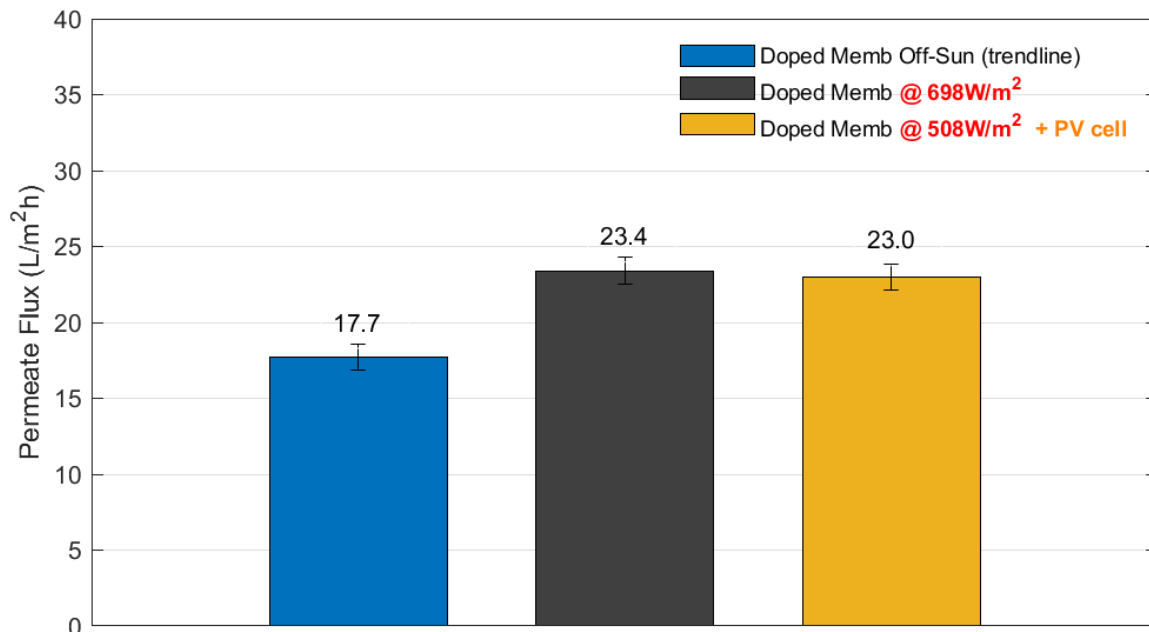


**Figure 3.18. Summary of the Solar Module (CdTe\_60%\_225) Effect on the Photothermal Effect of the Doped Membrane (C-Cu\_0.8\_Y\_250) at Standard Conditions**

**Table 3.3. Doped Membrane (C-Cu\_0.8\_Y\_250) and CdTe Thin Film Solar Module (CdTe\_60%\_225) Performances On-Sun at Standard Conditions**

Test Name	Feed Inlet Temp (°C)	Permeate Inlet Temp (°C)	Solar Flux (W/m <sup>2</sup> )	Permeate Flux (L/m <sup>2</sup> h)	Power Production (W)
<i>Doped Memb Off-Sun (1)</i>	53.0	18.9	0.0	19.1	0.0
<i>Doped Memb Off-Sun (2)</i>	52.9	19.1	0.0	18.2	0.0
<i>Doped Memb Off-Sun (3)</i>	52.6	19.2	0.0	18.2	0.0
<i>Doped Memb Off-Sun (4)</i>	52.3	19.5	0.0	19.1	0.0
<i>Doped Memb Off-Sun (5)</i>	52.1	19.5	0.0	19.1	0.0
<i>Doped Memb Off-Sun (6)</i>	51.9	19.6	0.0	19.1	0.0
<i>Doped Memb @ 698W/m<sup>2</sup> (1)</i>	55.6	25.1	754.9	24.3	0.0
<i>Doped Memb @ 698W/m<sup>2</sup> (2)</i>	55.4	25.1	740.8	24.3	0.0
<i>Doped Memb @ 698W/m<sup>2</sup> (3)</i>	55.7	25.5	722.4	22.5	0.0
<i>Doped Memb @ 698W/m<sup>2</sup> (4)</i>	57.0	25.8	708.3	21.7	0.0
<i>Doped Memb @ 698W/m<sup>2</sup> (5)</i>	57.0	26.3	692.8	22.5	0.0
<i>Doped Memb @ 698W/m<sup>2</sup> (6)</i>	56.5	26.3	670.2	26.9	0.0
<i>Doped Memb @ 508W/m<sup>2</sup> + PV cell (1)</i>	56.8	26.7	629.3	23.4	0.39
<i>Doped Memb @ 508W/m<sup>2</sup> + PV cell (2)</i>	57.1	26.9	598.3	22.5	0.38
<i>Doped Memb @ 508W/m<sup>2</sup> + PV cell (3)</i>	56.3	27.4	565.8	22.5	0.36

Test Name	Feed Inlet Temp (°C)	Permeate Inlet Temp (°C)	Solar Flux (W/m <sup>2</sup> )	Permeate Flux (L/m <sup>2</sup> h)	Power Production (W)
<i>Doped Memb @ 508W/m<sup>2</sup> + PV cell (4)</i>	56.0	27.6	530.5	24.3	0.34
<i>Doped Memb @ 508W/m<sup>2</sup> + PV cell (5)</i>	55.8	27.3	489.6	21.7	0.32
<i>Doped Memb @ 508W/m<sup>2</sup> + PV cell (6)</i>	56.3	27.7	447.3	23.4	0.29

As a final summary, Figure 3.19 exhibits the desalination performance of the proposed hybrid design off-sun and on-sun at standard conditions. Both plain (Plain\_0.0\_Y\_250) and doped (C-Cu\_0.8\_Y\_250) membranes, as well as the solar module (CdTe\_60%\_225) are included into this graph.

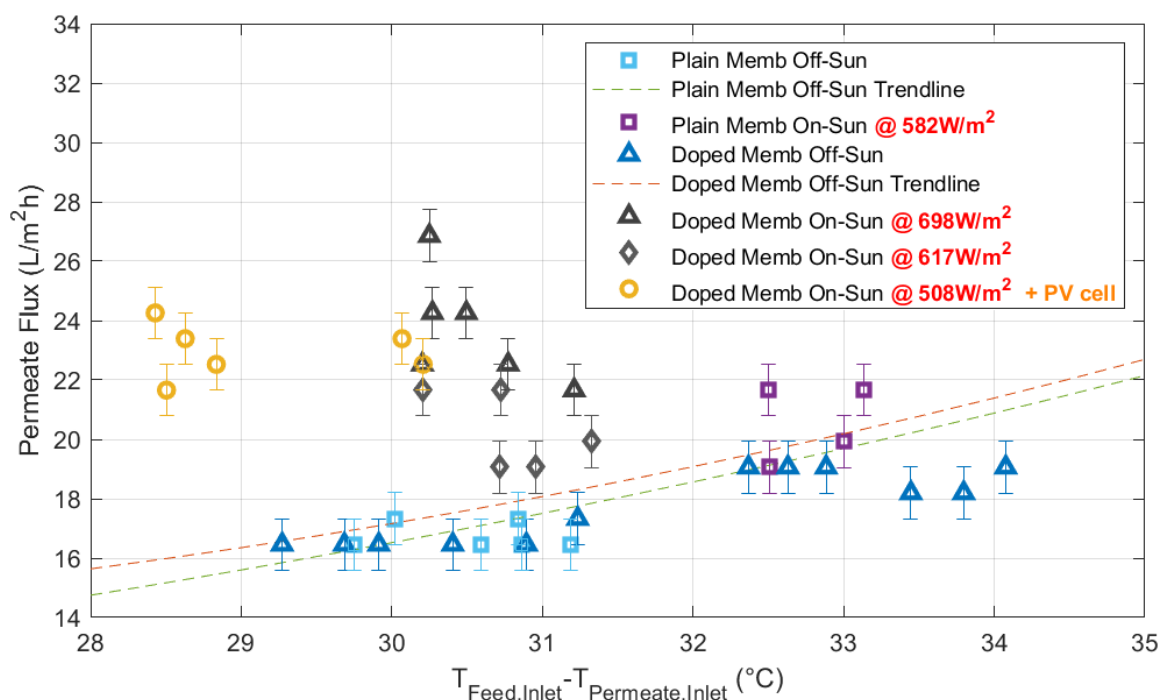


**Figure 3.19. Desalination Performance Summary of the Proposed Hybrid PV-Membrane System at Standard Conditions. Plain membrane (Plain\_0.0\_Y\_250), Doped membrane (C-Cu\_0.8\_Y\_250), and Solar Module (CdTe\_60%\_225)**

### 3.4. Conclusions

This chapter investigated the second high level objective of the study. First, a custom DCMD test setup, including the proposed hybrid PV-membrane module, was successfully built. Second, the system's characterization, including the solar module and multiple membranes, has been achieved through multiple indoor and outdoor tests.

The plain (Plain\_0.0\_Y\_250) and doped (C-Cu\_0.8\_Y\_250) membranes, characterized in this custom setup, displayed comparable performance during the off-sun testing. Both membranes demonstrated an enhancement of the desalination performance as the feed temperature increases due to a higher vapor pressure gradient between the feed and the permeate streams, which drives the desalination process. Moreover, both membranes improved their permeate flux as the stream's flow rate increases due to an enhancement of the turbulence, which decreases the thickness of the temperature boundary layer. On the other hand, both membranes demonstrated a reduction of the permeate flux as the feed stream concentration increases due to a reduced vapor pressure gradient. In addition, the membranes demonstrated suitability for MD applications by maintaining a salt rejection above 99.8% during all of the tests.

The doped membrane demonstrated a permeate flux improvement of 15-32% under the influence of solar irradiance. This enhancement is attributed to the addition of nanoparticles, capable of absorbing the solar irradiance and transforming it into heat via plasmonic heating. Plasmon resonance of the NPs confirms the mitigation of the temperature polarization effect, the principal drawback of membranes distillation, by increasing the membrane surface temperature and obtaining a higher vapor pressure gradient for evaporation. This result is confirmed by comparing it to the plain membrane.

In this case, the plain membrane demonstrated a 6% performance increase under the influence of solar irradiance due to the radiative heating effect.

Moreover, the incorporation of a solar module (CdTe\_60%\_225) on top of the membrane module did not significantly affect the membrane performance, which is attributed to the high transparency of the solar module. Despite the low efficiency of the solar module, custom design modules can be obtained for further performance enhancement. The results demonstrate the validity of the hybrid design constituted of a DCMD coupled with a PV cell.

## CHAPTER FOUR: CONCLUSIONS AND FUTURE WORK

### 4.1 Conclusions

The development of a hybrid design consisting of DCMD coupled with a PV cell has been demonstrated as a potential alternative to current desalination technologies. Membranes doped with nanoparticles via the custom phase inversion process can be applied to MD technology to enhance the water distillation performance while maintaining the water quality. Moreover, the co-production of fresh water and electricity has been demonstrated by combining in the same design a DCMD module and a PV cell.

The development of a custom process for the fabrication of membranes has been achieved via phase inversion. The process creates membranes suitable for distillation applications such as MD with the possibility for the addition of nanoparticles. The morphological characterization of the membranes demonstrated a microporous hydrophobic structure, and in the case of the doped membranes, uniform dispersion of nanoparticles. The contact angle measurements above  $100^\circ$  proved the hydrophobic nature of the membrane, and the SEM images proved a microporous sponge-like structure with a pore size diameter range of 100-200nm and a uniform dispersion of nanoparticles. Moreover, the optical characterization of the membranes demonstrated a solar absorptance enhancement of 76.9% due to the addition of nanoparticles.

The co-production of fresh water and electricity of the system has been achieved in a custom lab-scale DCMD configuration with the proposed PV-membrane module at

the core of the design. The membranes demonstrated a stable and high quality distillation for different MD operating conditions, including high saline water. Furthermore, the doped membranes proved a 15-32% distillation enhancement under solar irradiance. The nanoparticles exposed to irradiance exhibited a photothermal heating effect capable of mitigating the main drawback of MD, the temperature polarization. Moreover, coupling a semitransparent solar module to the membrane module demonstrated little or no effect on the membrane performance, while producing useful electrical power output.

#### **4.2. Future Work**

Although these membranes provide distillation rates similar to the literature results, some improvements can be applied. Synthesis of unsupported membranes suitable for MD has not been achieved due to shrinkage during the phase inversion process. Continuous development work of this process should focus on the fabrication of unsupported membranes capable of incorporating nanoparticles.

The hybrid system described in this study can also continue to be improved. The current system has been tested under irradiance less than one sun ( $1,000 \text{ W/m}^2$ ), which presents the opportunity to combine the design with concentrated solar irradiance. Incorporating a concentrating solar energy system could continue to enhance the co-production of electricity and fresh water of the hybrid system.

Additional work can focus on developing a heat and mass transfer model capable of replicating the distillation performance of the membranes introduced in this study. That simulation model could predict the system performance and scale the design to industrial applications. Moreover, the simulation model would help identify the best

combination of semitransparent solar module and membrane module for different field applications.

## REFERENCES

- [1] Drioli, Enrico, Aamer Ali, and Francesca Macedonio. 2015. "Membrane Distillation: Recent Developments and Perspectives." *Desalination* 356: 56–84.
- [2] Mahdi, Mohammad, A Shirazi, and Ali Kargari. 2015. "A Review on Applications of Membrane Distillation (MD) Process for Wastewater Treatment." *Journal of Membrane Science and Research* 1: 101–12.
- [3] <https://www.un.org/sustainabledevelopment/water-and-sanitation/>
- [4] Abu-Zeid, Mostafa Abd El Rady, Yaqin Zhang, Hang Dong, Lin Zhang, Huan Lin Chen, and Lian Hou. 2015. "A Comprehensive Review of Vacuum Membrane Distillation Technique." *Desalination* 356 (January 2015): 1–14.
- [5] <https://unesdoc.unesco.org/ark:/48223/pf0000244041>
- [6] Qtaishat, Mohammed Rasool, and Fawzi Banat. 2013. "Desalination by Solar Powered Membrane Distillation Systems." *Desalination* 308: 186–97.
- [7] <https://idadesal.org/>
- [8] Lawrence K. Wang, Jiaping Paul Chen, Yung-Tse Hung, Nazih K. Shamma. 2008. *Membrane and Desalination Technologies*.
- [9] Alkhudhiri, Abdullah, Naif Darwish, and Nidal Hilal. 2012. "Membrane Distillation: A Comprehensive Review." *Desalination* 287 (January): 2–18.
- [10] Al-Obaidani, Sulaiman, Efrem Curcio, Francesca Macedonio, Gianluca Di Profio, Hilal Al-Hinai, and Enrico Drioli. 2008. "Potential of Membrane Distillation in Seawater Desalination: Thermal Efficiency, Sensitivity Study and Cost Estimation." *Journal of Membrane Science* 323 (1): 85–98.

- [11] Servi, Amelia T., Jehad Kharraz, David Klee, Katie Notarangelo, Brook Eyob, Elena Guillen-Burrieza, Andong Liu, Hassan A. Arafat, and Karen K. Gleason. 2016. "A Systematic Study of the Impact of Hydrophobicity on the Wetting of MD Membranes." *Journal of Membrane Science* 520: 850–59.
- [12] AlMarzooqi, Faisal A., M. R. Bilad, and Hassan A. Arafat. 2016. "Development of PVDF Membranes for Membrane Distillation via Vapour Induced Crystallisation." *European Polymer Journal* 77: 164–73.
- [13] Guillen-Burrieza, E., M. O. Mavukkandy, M. R. Bilad, and H. A. Arafat. 2016. "Understanding Wetting Phenomena in Membrane Distillation and How Operational Parameters Can Affect It." *Journal of Membrane Science* 515: 163–74.
- [14] Wang, Peng, and Tai Shung Chung. 2015. "Recent Advances in Membrane Distillation Processes: Membrane Development, Configuration Design and Application Exploring." *Journal of Membrane Science* 474: 39–56.
- [15] Politano, Antonio, Pietro Argurio, Gianluca Di Profio, Vanna Sanna, Anna Cupolillo, Sudip Chakraborty, Hassan A. Arafat, and Efrem Curcio. 2017. "Photothermal Membrane Distillation for Seawater Desalination." *Advanced Materials (Deerfield Beach, Fla.)* 29 (2): 1–6.
- [16] Dongare, Pratiksha D., Alessandro Alabastri, Seth Pedersen, Katherine R. Zodrow, Nathaniel J. Hogan, Oara Neumann, Jinjian Wu, et al. 2017. "Nanophotonics-Enabled Solar Membrane Distillation for off-Grid Water Purification." *Proceedings of the National Academy of Sciences*.
- [17] Chernyshov, M. N., G. W. Meindersma, and A. B. de Haan. 2005. "Comparison of Spacers for Temperature Polarization Reduction in Air Gap Membrane Distillation." *Desalination* 183 (1–3): 363–74.
- [18] Cath, Tzahi Y., V. Dean Adams, and Amy E. Childress. 2004. "Experimental Study of Desalination Using Direct Contact Membrane Distillation: A New Approach to Flux Enhancement." *Journal of Membrane Science* 228 (1): 5–16.

- [19] Manawi, Yehia M., Majeda A.M.M. Khraisheh, Ahmad Kayvani Fard, Farid Benyahia, and Samer Adham. 2014. "A Predictive Model for the Assessment of the Temperature Polarization Effect in Direct Contact Membrane Distillation Desalination of High Salinity Feed." *Desalination* 341 (1): 38–49.
- [20] Franken, A. C.M., J. A.M. Nolten, M. H.V. Mulder, D. Bargeman, and C. A. Smolders. 1987. "Wetting Criteria for the Applicability of Membrane Distillation." *Journal of Membrane Science* 33 (3): 315–28.
- [21] Lalia, Boor Singh, Elena Guillen-Burrieza, Hassan A. Arafat, and Raed Hashaikeh. 2013. "Fabrication and Characterization of Polyvinylidene fluoride-Co-Hexafluoropropylene (PVDF-HFP) Electrospun Membranes for Direct Contact Membrane Distillation." *Journal of Membrane Science* 428: 104–15.
- [22] Smolders, K., and A. C.M. Franken. 1989. "Terminology for Membrane Distillation." *Desalination* 72 (3): 249–62.
- [23] Srisurichan, Surapit, Ratana Jiratananon, and A. G. Fane. 2006. "Mass Transfer Mechanisms and Transport Resistances in Direct Contact Membrane Distillation Process." *Journal of Membrane Science* 277 (1–2): 186–94.
- [24] Tijing, Leonard D., Yun Chul Woo, Wang Geun Shim, Tao He, June Seok Choi, Seung Hyun Kim, and Ho Kyong Shon. 2016. "Superhydrophobic Nanofiber Membrane Containing Carbon Nanotubes for High-Performance Direct Contact Membrane Distillation." *Journal of Membrane Science* 502: 158–70.
- [25] Feng, C. Y., K. C. Khulbe, T. Matsuura, and A. F. Ismail. 2013. "Recent Progresses in Polymeric Hollow Fiber Membrane Preparation, Characterization and Applications." *Separation and Purification Technology* 111 (May): 43–71.
- [26] Vanherck, Katrien, Ivo Vankelecom, and Thierry Verbiest. 2011. "Improving Fluxes of Polyimide Membranes Containing Gold Nanoparticles by Photothermal Heating." *Journal of Membrane Science* 373 (1–2): 5–13.

- [27] Prince, J. A., G. Singh, D. Rana, T. Matsuura, V. Anbharasi, and T. S. Shanmugasundaram. 2012. "Preparation and Characterization of Highly Hydrophobic Poly(Vinylidene Fluoride) - Clay Nanocomposite Nanofiber Membranes (PVDF-Clay NNMs) for Desalination Using Direct Contact Membrane Distillation." *Journal of Membrane Science* 397–398: 80–86.
- [28] Boo, Chanhee, Jongho Lee, and Menachem Elimelech. 2016. "Engineering Surface Energy and Nanostructure of Microporous Films for Expanded Membrane Distillation Applications." Research-article. *Environmental Science and Technology* 50 (15): 8112–19.
- [29] Lee, Eui Jong, Alicia Kyoungjin An, Tao He, Yun Chul Woo, and Ho Kyong Shon. 2016. "Electrospun Nanofiber Membranes Incorporating Fluorosilane-Coated TiO<sub>2</sub> Nanocomposite for Direct Contact Membrane Distillation." *Journal of Membrane Science* 520: 145–54.
- [30] Thakur, Vijay Kumar, Meng Fang Lin, Eu Jin Tan, and Pooi See Lee. 2012. "Green Aqueous Modification of Fluoropolymers for Energy Storage Applications." *Journal of Materials Chemistry* 22 (13): 5951–59.
- [31] Blanco Gálvez, Julián, Lourdes García-Rodríguez, and Isabel Martín-Mateos. 2009. "Seawater Desalination by an Innovative Solar-Powered Membrane Distillation System: The MEDESOL Project." *Desalination* 246 (1–3): 567–76.
- [32] Calise, Francesco, Massimo Dentice d'Accadia, and Antonio Piacentino. 2014. "A Novel Solar Trigeneration System Integrating PVT (Photovoltaic/Thermal Collectors) and SW (Seawater) Desalination: Dynamic Simulation and Economic Assessment." *Energy* 67: 129–48.
- [33] Summers, Edward Kurt, Ryan Enright, and John H Lienhard. 2013. "SOLAR-DRIVEN AIR GAP MEMBRANE DISTILLATION SYSTEM." *United States Patent Application Publication*.
- [34] Termpiyakul, P., Ratana Jiraratananon, and S. Srisurichan. 2005. "Heat and Mass Transfer Characteristics of a Direct Contact Membrane Distillation Process for Desalination." *Desalination* 177 (1–3): 133–41.

- [35] Martínez-Díez, L., and M. I. Vázquez-González. 2000. "A Method to Evaluate Coefficients Affecting Flux in Membrane Distillation." *Journal of Membrane Science* 173 (2): 225–34.
- [36] Alsaadi, Ahmad S., Lijo Francis, Gary L. Amy, and Noredine Ghaffour. 2014. "Experimental and Theoretical Analyses of Temperature Polarization Effect in Vacuum Membrane Distillation." *Journal of Membrane Science* 471: 138–48.
- [37] Vanherck, Katrien, Sanne Hermans, Thierry Verbiest, and Ivo Vankelecom. 2011. "Using the Photothermal Effect to Improve Membrane Separations via Localized Heating." *Journal of Materials Chemistry* 21 (16): 6079–87.
- [38] Politano, A., A. Cupolillo, G. Di Profio, H. A. Arafat, G. Chiarello, and E. Curcio. 2016. "When Plasmonics Meets Membrane Technology." *Journal of Physics Condensed Matter* 28 (36).
- [39] Li, Yanbo, Thierry Verbiest, and Ivo Vankelecom. 2013. "Improving the Flux of PDMS Membranes via Localized Heating through Incorporation of Gold Nanoparticles." *Journal of Membrane Science* 428: 63–69.
- [40] Li, Yanbo, Thierry Verbiest, Rik Strobbe, and Ivo F J Vankelecom. 2014. "Silver Nanoparticles as Localized 'Nano-Heaters' under LED Light Irradiation to Improve Membrane Performance." *Journal of Materials Chemistry A* 2 (9): 3182–89.
- [41] Politano, Antonio, Gianluca Di Profio, Enrica Fontananova, Vanna Sanna, Anna Cupolillo, and Efram Curcio. 2018. "Overcoming Temperature Polarization in Membrane Distillation by Thermoplasmonic Effects Activated by Ag Nanofillers in Polymeric Membranes." *Desalination* 451 (October 2017): 192–99.
- [42] Lind, Mary Laura. 2018. "Nanophotonic Pervaporation Desalination," no. 213.
- [43] Bergerud, Amy, Dennis Nordlund, Evan L. Runnerstrom, Delia J. Milliron, and Sebastien D. Lounis. 2014. "Influence of Dopant Distribution on the Plasmonic Properties of Indium Tin Oxide Nanocrystals." *Journal of the American Chemical Society* 136 (19): 7110–16.

- [44] S.J. Oldenburg, R.D. Averitt, S.L. Westcott, N.J. Halas. 1998. "Nanoengineering of Optical Resonances." *Journal of Communicable Diseases* 19 (1): 86–88.
- [45] Halas, Naomi. 2005. "Playing with Plasmons: Tuning the Optical Resonant Properties of Metallic Nanoshells." *MRS Bulletin* 30 (5): 362–67.
- [46] Knight, Mark W., and Naomi J. Halas. 2008. "Nanoshells to Nanoeggs to Nanocups: Optical Properties of Reduced Symmetry Core-Shell Nanoparticles beyond the Quasistatic Limit." *New Journal of Physics* 10.
- [47] Yu, Yu Ying, Ser Sing Chang, Chien Liang Lee, and C. R. Chris Wang. 1997. "Gold Nanorods: Electrochemical Synthesis and Optical Properties." *Journal of Physical Chemistry B* 101 (34): 6661–64.
- [48] Jain, Prashant K, Kyeong Seok Lee, Ivan H El-sayed, and Mostafa A El-sayed. 2006. "Calculated Absorption and Scattering Properties of Gold Nanoparticles of Different Size, Shape, and Composition: Applications in Biological Imaging and Biomedicine," 7238–48.
- [49] Roshani, Ramin, Fatemeh Ardeshiri, Majid Peyravi, and Mohsen Jahanshahi. 2018. "Highly Permeable PVDF Membrane with PS/ZnO Nanocomposite Incorporated for Distillation Process." *RSC Advances* 8 (42): 23499–515.
- [50] Otanicar, Todd, Bryan Kinzer, and Kirk Smith. 2018. "HYBRID SOLAR ENERGY / DESALINATION USING SPECTRALLY SELECTIVE MEMBRANE DISTILLATION," 1–8.
- [51] Bilad, Muhammad R., Elena Guillen-Burrieza, Musthafa O. Mavukkandy, Faisal A. Al Marzooqi, and Hassan A. Arafat. 2015. "Shrinkage, Defect and Membrane Distillation Performance of Composite PVDF Membranes." *Desalination* 376: 62–72.
- [52] Dobrak-Van Berlo, Agnieszka, Ivo F.J. Vankelecom, and Bart Van der Bruggen. 2011. "Parameters Determining Transport Mechanisms through Unfilled and Silicalite Filled PDMS-Based Membranes and Dense PI Membranes in Solvent Resistant Nanofiltration: Comparison with Pervaporation." *Journal of Membrane Science* 374 (1–2): 138–49.

- [53] DeJarnette, Drew, Todd Otanicar, Nick Brekke, Parameswar Hari, and Kenneth Roberts. 2015. "Selective Spectral Filtration with Nanoparticles for Concentrating Solar Collectors." *Journal of Photonics for Energy* 5 (1): 057008.
- [54] Otanicar, Todd P., Patrick E. Phelan, Ravi S. Prasher, Gary Rosengarten, and Robert A. Taylor. 2010. "Nanofluid-Based Direct Absorption Solar Collector." *Journal of Renewable and Sustainable Energy* 2 (3).
- [55] Taylor, Robert A., Patrick E. Phelan, Todd P. Otanicar, Himanshu Tyagi, and Steven Trimble. 2011. "Applicability of Nanofluids in Concentrated Solar Energy Harvesting," 825–32.
- [56] Khayet, M., and T. Matsuura. 2001. "Preparation and Characterization of Polyvinylidene Fluoride Membranes for Membrane Distillation." *Industrial and Engineering Chemistry Research* 40 (24): 5710–18.
- [57] Fontananova, Enrica, Johannes C. Jansen, Alessandra Cristiano, Efrem Curcio, and Enrico Drioli. 2006. "Effect of Additives in the Casting Solution on the Formation of PVDF Membranes." *Desalination* 192 (1–3): 190–97.
- [58] Wei, Yong, Hua Qiang Chu, Bing Zhi Dong, Xuan Li, Sheng Ji Xia, and Zhi Min Qiang. 2011. "Effect of TiO<sub>2</sub>nanowire Addition on PVDF Ultrafiltration Membrane Performance." *Desalination* 272 (1–3): 90–97.
- [59] Meringolo, Carmen, Teresa F. Mastropietro, Teresa Poerio, Enrica Fontananova, Giovanni De Filpo, Efrem Curcio, and Gianluca Di Profio. 2018. "Tailoring PVDF Membranes Surface Topography and Hydrophobicity by a Sustainable Two-Steps Phase Separation Process." *ACS Sustainable Chemistry and Engineering* 6 (8): 10069–77.
- [60] Hagen, Kirk D. Heat transfer with applications. Prentice Hall, 1999.